

JADES - The small blue bump in GN-z11: insights into the nuclear region of a galaxy at z=10.6

Xihan Ji,^{1,2*} Roberto Maiolino,^{1,2,3} Gary Ferland,⁴ Francesco D’Eugenio,^{1,2} Rachana Bhatawdekar,⁵ Stéphane Charlot,⁶ Jacopo Chevallard,⁷ Mirko Curti,⁸ Emma Curtis-Lake,⁹ Kevin Hainline,¹⁰ Zhiyuan Ji,¹⁰ Brant Robertson,¹¹ Bruno Rodríguez Del Pino,¹² Jan Scholtz,^{1,2} Sandro Tacchella,^{1,2} Christina C. Williams,¹³ Joris Witstok^{1,2}

¹Kavli Institute for Cosmology, University of Cambridge, Madingley Road, Cambridge, CB3 0HA, UK

²Cavendish Laboratory, University of Cambridge, 19 JJ Thomson Avenue, Cambridge, CB3 0HE, UK

³Department of Physics and Astronomy, University College London, Gower Street, London WC1E 6BT, UK

⁴Department of Physics and Astronomy, University of Kentucky, 505 Rose Street, Lexington, KY 40506, USA

⁵European Space Agency (ESA), European Space Astronomy Centre (ESAC), Camino Bajo del Castillo s/n, 28692 Villanueva de la Cañada, Madrid, Spain

⁶Sorbonne Université, CNRS, UMR 7095, Institut d’Astrophysique de Paris, 98 bis bd Arago, 75014 Paris, France

⁷Department of Physics, University of Oxford, Denys Wilkinson Building, Keble Road, Oxford OX1 3RH, UK

⁸European Southern Observatory, Karl-Schwarzschild-Strasse 2, 85748 Garching, Germany

⁹Centre for Astrophysics Research, Department of Physics, Astronomy and Mathematics, University of Hertfordshire, Hatfield AL10 9AB, UK

¹⁰Steward Observatory, University of Arizona, 933 N. Cherry Avenue, Tucson, AZ 85721, USA

¹¹Department of Astronomy and Astrophysics University of California, Santa Cruz, 1156 High Street, Santa Cruz CA 96054, USA

¹²Centro de Astrobiología (CAB), CSIC–INTA, Cra. de Ajalvir Km. 4, 28850- Torrejón de Ardoz, Madrid, Spain

¹³NSF’s National Optical-Infrared Astronomy Research Laboratory, 950 North Cherry Avenue, Tucson, AZ 85719, USA

21 May 2024

ABSTRACT

We report the detection of continuum excess in the rest-frame UV between 3000 Å and 3550 Å in the JWST/NIRSpec spectrum of GN-z11, a galaxy hosting an active galactic nucleus (AGN) at $z = 10.603$. The shape of the continuum excess resembles a Balmer continuum but has a break around 3546 Å in the rest frame, which is 100 Å bluewards to the Balmer limit at 3646 Å. A Balmer continuum model alone cannot fit the spectrum, implying a different origin for the continuum excess. The absence of the Balmer jump indicates an electron temperature of $\sim 3 \times 10^4$ K, which is significantly higher than the temperature of $T_e(\text{O}^{2+}) \approx 1.3 \times 10^4$ K inferred from $[\text{O III}]\lambda 4363$. The temperature difference must result from mixing of different ionized regions: the Balmer emission mainly arises from dense and hot clouds in the Broad Line Region, close to the accreting black hole, whereas the forbidden lines originate from less dense and colder gas, associated either with the Narrow Line Region or the InterStellar Medium ionized by star formation in the host galaxy (although BLR and NLR/ISM are kinematically similar in GN-z11 due to its small BH mass). We propose a potential explanation for the observed continuum excess to come from a complex of Fe II emission, which shows a characteristic jump bluewards to the Balmer limit as previously seen in the spectra of many lower-redshift quasars. Through comparisons with CLOUDY models, we show an Fe abundance or an overall metallicity above $\sim 1/3$ solar is likely needed. Such a high Fe abundance can be achieved via enrichment from Type-Ia supernovae (although unlikely at such early times), hypernovae, or pair-instability supernovae. Besides the Fe II emission, part of the small blue bump might also be associated with an O III Bowen fluorescent line, a line often enhanced in dense AGN-ionized gas. Finally, the spectrum provides further evidence against Wolf-Rayet or massive stars dominating the nebular emission in GN-z11.

Key words: galaxies: abundances – galaxies: active – galaxies: evolution – galaxies: high-redshift

1 INTRODUCTION

The UV spectra of Type-1 active galactic nuclei (AGNs) often show prominent continuum excess extending from 2000 Å to 4000 Å, which is also known as the “3000 Å excess” or the “small blue bump” (Neugebauer et al. 1979; Richstone & Schmidt 1980; Grandi 1982). Early observations show the small blue bumps in quasars exhibit a

variety of shapes and are found to show variability weakly correlated with that of the UV continuum (e.g., Ulrich et al. 1980, 1997). In addition, polarization analyses of the spectrum of the Seyfert-1 galaxy NGC 4151 show the small blue bump has a similar polarization as that of broad emission lines, implying a photoionization origin in the broad-line region (BLR; Schmidt & Miller 1980).

The commonly adopted explanation for the UV continuum excess is a combination of Fe II emission and Balmer continuum (e.g., Grandi 1981, 1982; Malkan & Sargent 1982; Wills et al. 1985; Diet-

* E-mail: xj274@cam.ac.uk

rich et al. 2003; Kovačević et al. 2014). In BLRs, collisional excitation of Fe^+ , fluorescence by Fe II lines as well other emission lines with similar wavelengths, and radiative excitation by the AGN continuum are able to produce strong Fe II emission (Netzer & Wills 1983; Wills et al. 1985; Penston 1987). Another important factor that enables detectable Fe II emission in BLRs is the sublimation of dust grains, as Fe is usually significantly depleted onto dust in the interstellar medium (ISM; Jenkins 2009). However, it is also suggested that the varying strength of Fe II in observations might indicate the occasional overlap of the Fe II emitting region with regions outside the dust sublimation radius (Shields et al. 2010). Due to the dense energy levels of Fe^+ and fast motions of clouds within BLRs, Fe II emission lines are usually highly blended in observations and form a pseudo-continuum spanning from the rest-frame UV to optical. Still, in both observations and theoretical models of the Fe II pseudo-continuum, the Fe II emission can be divided by groups of broad emission centering at different wavelengths, whose relative strengths are determined by a series parameters including the optical depth, the velocity of microturbulence, the metallicity, and so forth (e.g., Baldwin et al. 2004; Ferland et al. 2009; Sarkar et al. 2021). The edges of the Fe II groups, especially between the UV groups and optical groups, are prominent in some quasar spectra and resemble sharp jumps in the pseudo-continuum excess (e.g., Tsuzuki et al. 2006).

Besides the Fe II emission, a Balmer continuum is often needed for a complete fit of the UV spectra of Type-1 AGNs. The Balmer continuum contributes to a smoothly rising component of the continuum until the Balmer limit at 3646 \AA . The Balmer continuum is produced by the recombination of free electrons to the $n = 2$ level of hydrogen. The presence of the Balmer continuum provides an independent probe of the gas temperature. This is because the ratio between the intensity of the Balmer continuum at the Balmer limit and that of any given Balmer line decreases with increasing temperature roughly following a power-law relation (Peimbert 1967). As temperature increases, while the whole nebular continuum becomes stronger, the relative strength of the Balmer jump becomes weaker with respect to the intensity of Balmer lines. According to the widely adopted BLR model with a stratified ionization structure, H I emission including the Balmer continuum comes from clouds closer to the accretion disk compared to Fe II emission, leading to the stronger variability of H I emission in observations (Ulrich et al. 1997).

Understanding the origin of the small blue bump and decomposing the contributions from different nebular emissions are important for constraining the Fe abundance as well as the electron temperature of the BLR. While the flux ratio of $\text{Mg II } \lambda\lambda 2796, 2803 / \text{Fe II}$ measured in the rest-frame UV has been used as an empirical proxy of the abundance ratio of α / Fe in Type-1 AGNs, the accurate determination of the Fe abundance requires detailed modeling of the physical conditions within BLRs (Maiolino & Mannucci 2019). Previous theoretical modeling attempts have shown it is particularly challenging to reproduce the various strengths of the observed Fe II complex (Gaskell et al. 2022). Although significant progress has been made by implementing complex energy levels of Fe^+ as well as physical processes such as self fluorescence and continuum pumping in photoionization simulations, the current application of the theoretical approach is limited to a few well observed sources and certain parameter regimes (e.g., I Zwicky 1; Sarkar et al. 2021). As the UV spectrum becomes increasingly important for spectroscopic studies of AGNs in the early Universe, it is vital to understand the UV signatures of AGNs over a broader parameter space. On the other hand, independent temperature determinations from the Balmer jump can provide important clues on the temperature structures and chemical abundance patterns in AGNs. The main limiting factor for constrain-

ing the Balmer temperature in BLRs, however, is the degeneracy between the strength of the Balmer continuum and that of the Fe II complex.

With the advent of the James Webb Space Telescope (JWST; Gardner et al. 2023; Rigby et al. 2023), a diverse population of AGNs has been revealed at $z \sim 2 - 11$ (Furtak et al. 2023; Greene et al. 2023; Kocevski et al. 2023; Maiolino et al. 2024b, 2023b; Matthee et al. 2023; Onoue et al. 2023; Scholtz et al. 2023b; Übler et al. 2023a,b). Meanwhile, emission-line studies based on JWST/NIRSpec (Jakobsen et al. 2022) have shown the prevalence of highly ionized and metal-poor gas in the early Universe (e.g., Cameron et al. 2023a; Curti et al. 2023a,b; Laseter et al. 2023; Sanders et al. 2023a,b; Tacchella et al. 2023a). At this parameter regime, the behavior of the small blue bump remains unexplored. A naive expectation might be that the small blue bump becomes less important and even vanishes in the BLRs of very early AGNs because of low Fe abundances and high electron temperatures. However, in this manuscript we report the discovery of a significantly detected UV continuum excess in the JWST/NIRSpec spectrum of GN-z11, a luminous galaxy hosting an AGN $z = 10.603$ (Oesch et al. 2016; Bunker et al. 2023b; Tacchella et al. 2023b; Maiolino et al. 2024b), which partly resembles the shape of the small blue bumps previously observed in lower-redshift AGNs. This “small blue bump” raises questions about whether the chemical enrichment processes and temperature structures in early AGNs differ from those at later cosmic epochs. We show that such a bump is inconsistent with being associated with a Balmer jump; this implies that the temperature associated with the Balmer lines must be much higher than that inferred from the auroral (forbidden) transition, $[\text{O III}] \lambda 4363$, further confirming that the Balmer lines predominantly come from the BLR. We then interpret the small bump similarly as in other Type-1 AGNs (i.e., associated with the Fe complex, although likely with different properties relative to local AGN).

The layout of the manuscript is as follows. In Section 2, we describe the observational data we use. In Section 3, we introduce our method to analyze the observed continuum. In Sections 4 to 7, we compare the observed UV continuum excess with nebular emission models as well as previously observed broad-line AGN spectra to identify potential contributions from the Balmer continuum, Fe II emission, and other nebular emission. We discuss the physical interpretations for the shape and variation of the UV continuum excess as well as the temperature structures in the ionized clouds in Section 8. We also comment on potential emission from other atoms and ions in this wavelength regime. In Section 9, we present our conclusions and outlooks.

2 OBSERVATIONAL DATA AND MAIN SPECTRAL FEATURES

In this work we use observational data obtained by JWST/NIRSpec. Our sample galaxy, GN-z11, was originally detected by the Hubble Space Telescope (HST) in the CANDELS GOODS North field (Grogin et al. 2011; Koekemoer et al. 2011; Oesch et al. 2016) and was later observed in the JWST Advanced Deep Extragalactic Survey (JADES) under the Cycle 2 Program ID 1181 (P.I.: D. Eisenstein; Eisenstein et al. 2023a). The spectrum was obtained by combining observations from two different epochs and the detailed descriptions of the observations and data reduction are given by Bunker et al. (2023b) and Maiolino et al. (2024b). In brief, there are two sets of observations obtained in February 2023 and May 2023, respectively. The February observation consists of four NIRSpec micro-shutter assembly (MSA; Jakobsen et al. 2022; Ferruit et al. 2022; Böker et al.

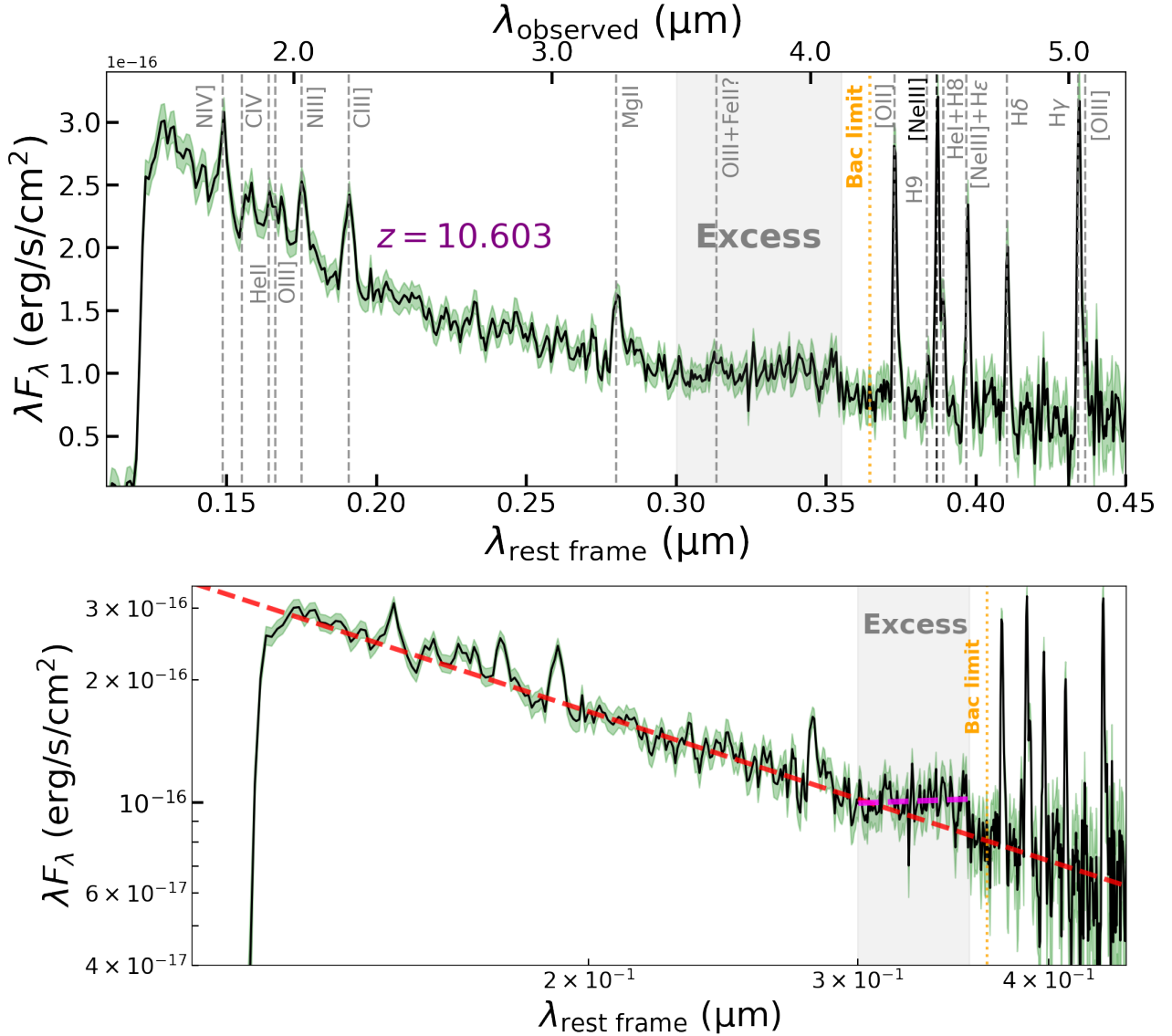


Figure 1. *Top:* NIRSpec/Prism spectrum of GN-z11. Locations of detected UV and optical emission lines are marked by vertical dashed grey lines. Near the location of C IV, there are both a blueshifted absorption trough and a redshifted emission feature, indicating the presence of outflow (Maiolino et al. 2024b). The grey shaded band indicates the visually identified spectral region showing continuum excess. The orange dotted line indicates the location of the Balmer continuum (Bac) limit at 3646 Å. *Bottom:* the same spectrum plotted on a log scale. We also plotted two power-law functions that fit the spectrum excluding major emission lines and the continuum excess (red dashed line) and the continuum excess only (magenta dashed line), respectively.

2023) configurations, with 14 groups per integration, one integration per exposure, and three nods each. Each configuration was repeated two times, for a total of 6.9 hr exposure time. The May observation consists of three MSA configurations, again with 14 groups per integration, one integration per exposure and three nods, but each configuration was used only one time, for a total of 2.6 hr exposure time.

Figure 1 shows the 1D NIRSpec/Prism spectrum of GN-z11, where we marked locations of prominent emission lines. We measured the fluxes of important emission lines including H γ , H δ , [O III] λ 4363, [Ne III] λ 3869, and [O II] λ 3726, 3729 in the Prism spectrum for the derivation of the electron temperature and oxygen abundance. To measure the emission lines, we used the penalized pixel-fitting code (pPXF; Cappellari & Emsellem 2004; Cappellari 2017) and fitting emission lines as Gaussians. During the fit, we tied the kin-

ematics of Balmer lines and forbidden lines separately to account for their potentially different origins in the galaxy. To estimate the flux uncertainties, we manually added noise to the original spectrum according to the values reported by the data reduction pipeline and then refitted emission lines. The above procedure was repeated 500 times and for each emission line, we took the 68% confidence interval of the flux distribution and divided it by $2\sqrt{2}$ to obtain the final uncertainty estimate¹. We compared our flux measurements with those by Bunker et al. (2023b) and Maiolino et al. (2024b) and confirmed good consistency.

To correctly interpret the physical conditions of the ionized ISM, it is critical to identify the dominant ionizing source (Kewley et al.

¹ The scaling factor of $2\sqrt{2}$ is motivated by the fact that the total noise has been enlarged by a factor of $\sqrt{2}$ after adding noise to the observed spectrum.

2019; Maiolino & Mannucci 2019). In the case of GN-z11, one can see prominent high-ionization semi-forbidden transitions of nitrogen including N III] multiplets around 1750 Å and N IV]λ1487 Å in the Prism spectrum, which can further be separated in the medium-resolution Grating spectrum. A careful analysis on the multiplet ratios of N III] and N IV] indicates a high electron density of $n_e \gtrsim 10^9 \text{ cm}^{-3}$, typical of the physical conditions in BLRs while unseen in the ISM (Maiolino et al. 2024b). The AGN identification is furthermore confirmed by the detection of transitions typical of AGN, such as the C II*1335 fluorescent emission and [Ne IV], high velocities ionized winds seen in C IV (Maiolino et al. 2024b), ionization cones in C III] (Maiolino et al. 2023a), and an extended Lyα halo, whose brightness and extent is consistent with what observed in high-*z* quasars and inconsistent with simple star forming galaxies (Scholtz et al. 2023a). The measured widths of permitted lines are narrower than those typically found in lower-*z* Type-1 AGNs, but in the range of those seen in the so-called Narrow Line Seyfert 1s (NLSy1s; Osterbrock & Pogge 1985; Goodrich 1989; Leighly 1999), and compatible with a low-mass black hole with $M_{\text{BH}} \sim 1.6 \times 10^6 M_{\odot}$. Meanwhile, Maiolino et al. (2024b) estimated an Eddington ratio of 5 (with an uncertainty of a factor of 2), further confirming that GN-z11 is similar to NLSy1s. It is worth noticing, in the context of this paper, that NLSy1s tend to show prominent Fe II emissions (e.g., Véron-Cetty et al. 2001; Vestergaard & Wilkes 2001; Komossa 2008). Interestingly, the existence of strong nitrogen lines suggests a super-solar N/O ~ 430 Myr after the Big Bang, indicative of either a exotic chemical enrichment history in this galaxy or a past chemical enrichment within the small BLR (Bunker et al. 2023b; Cameron et al. 2023b; Maiolino et al. 2024b; Senchyna et al. 2023). Since the first Type-Ia supernovae (SNe) that are capable of enriching Fe can occur as early as ~ 30 Myr after the initial star formation (e.g., Maiolino & Mannucci 2019), if there has been past chemical enrichment in the BLR, one might expect Fe has also been enriched by a few SNe given the likely active star formation in GN-z11 over the past 20–50 Myr (Tacchella et al. 2023b).

In addition to the several emission lines identified in the previous studies, the spectrum of GN-z11 also shows a clear excess above the simple power law continuum, roughly between 3000 Å and 3550 Å in the rest frame. We marked the region showing the continuum excess in Figure 1, where the spectrum is plotted both in linear (top panel) and logarithmic (bottom panel) scales. To demonstrate the significance of the excess, we fit two power-law functions to the continuum excluding major emission lines (with at least ~ 30 Å space around each emission line) and the excess region and the excess region only.

The best-fit power-law functions follow $F_{\lambda} \propto \lambda^{-2.21 \pm 0.04}$ for the majority of the continuum, and $F_{\lambda} \propto \lambda^{-0.86 \pm 0.22}$ for the excess region. Although the pixel-wise differences between the continuum excess and the power law followed by the majority of the continuum are mostly on the level of 1σ , the cumulative difference over the 550 Å spectral window of the continuum excess is 7.8σ .

To check whether the bump is driven by any artefact in observations, we Jackknifed the Prism spectra using individual measurements and still found significant continuum excess. We show the Jackknifed spectra in Appendix A.

Such flattening of the continuum is expected if a Balmer continuum exists and dominates the part of the continuum close to the Balmer limit. However, as shown by Figure 1, the Balmer limit is ~ 100 Å (or 19 pixels) redwards to the observed edge of the continuum excess, hence excluding that the excess is associated with the Balmer continuum. Fe II emission, on the other hand, could contribute to the flattening of the observed continuum as well. However, typical UV

Fe II emission in quasars show larger intensities bluewards to 3000 Å rather than redwards to 3000 Å (e.g., Tsuzuki et al. 2006). Nevertheless, the physical conditions in this early galaxy could be drastically different from the lower redshift quasars given its low-mass and actively accreting black hole as well as its peculiar abundance pattern. Therefore, we speculate its Fe II emission could also have different shapes compared to those typically seen lower redshift AGNs. We note that besides the Balmer continuum and the Fe II complex, the spectral window between 3000 Å and 3550 Å usually lacks strong nebular emission in both observations and simulations.

In the next section, we outline our method to fit different continuum components in the Prism spectrum of GN-z11 and evaluate the goodness of fits based on different assumptions. We then exclude more quantitatively that the bump is associated with a Balmer continuum, hence deriving constraints for the BLR temperature, and then propose the interpretation in terms of Fe complex.

3 METHODOLOGY

To characterize the observed UV continuum of GN-z11, we considered three major components summarized below.

(i) A power law continuum that follows $F_{\lambda} = \alpha\lambda^{\beta}$, corresponding to the thermal emission from the AGN accretion disk (the “big blue bump”) or the UV continuum of young stellar populations. While the UV continua of early galaxies might also have contributions from two-photon emission (Cameron et al. 2023a), based on the high electron density inferred from N III] and N IV] (Maiolino et al. 2023b), we did not consider the hydrogen two-photon continuum due to its low critical density ($\sim 10^3 \text{ cm}^{-3}$; Bottorff et al. 2006). Also, F_{λ} does not peak at ~ 1430 Å as would be the case if a two-photon continuum dominated the UV spectrum (Gaskell 1980).

(ii) A Balmer continuum truncated at 3646 Å. We considered an optically thin Balmer continuum that follows

$$F_{\lambda} = F_{\lambda}^{\text{BE}} \left(\frac{\lambda_{\text{BE}}}{\lambda} \right)^2 e^{-\frac{hc}{k_B T_e} \left(\frac{1}{\lambda} - \frac{1}{\lambda_{\text{BE}}} \right)}; \lambda \leq \lambda_{\text{BE}}, \quad (1)$$

where BE means the Balmer continuum edge and $\lambda_{\text{BE}} = 3646$ Å. The only free parameter is the electron temperature, T_e . At fixed T_e , the flux at the Balmer edge, F_{λ}^{BE} , is set by the measured fluxes of Balmer lines. In our case, we used the strongest available Balmer line, Hγ, and computed a series of CLOUDY (c17.03; Ferland et al. 2017) models to relate the model predicted $\lambda_{\text{BE}} F_{\lambda}^{\text{BE}}$ to the volume-average T_e over a range of $10^4 \text{ K} \leq T_e \leq 3 \times 10^4 \text{ K}$ assuming the optically thin limit for the Balmer continuum. We discuss an alternative choice of a partially optically thick Balmer continuum as initially suggested by Grandi (1982) for fitting quasar spectra in Appendix B. We note that our main conclusions do not depend on the choice of the Balmer continuum model.

(iii) An Fe II complex in the UV. We computed CLOUDY Fe II models assuming a range of parameters listed in Table 1, which are typical parameters used to model nebular emission from BLRs (e.g., Verner et al. 1999; Baldwin et al. 2004; Ferland et al. 2009; Sarkar et al. 2021). Specifically, we used a standard AGN spectral energy distribution (SED) with a big blue bump temperature of $T_{\text{BB}} = 10^6 \text{ K}$, a UV-to-X-ray slope of $\alpha_{\text{ox}} = -1.4$, a UV slope of $\alpha_{\text{uv}} = -0.5$, and an X-ray slope of $\alpha_{\text{x}} = -1.0$. The full SED is described by the following function

$$F_{\nu} = \nu^{\alpha_{\text{uv}}} \exp(-h\nu/kT_{\text{BB}}) \exp(0.01 \text{ Ryd}/h\nu) + a\nu^{\alpha_{\text{x}}}, \quad (2)$$

where a is automatically adjusted by CLOUDY to produce the preset

Table 1. Input parameters for CLOUDY Fe II models

Parameter	Values
SED	$T_{\text{BB}} = 10^6$ K, $\alpha_{\text{ox}} = -1.4$, $\alpha_{\text{uv}} = -0.5$, $\alpha_x = -1.0$
$\log(U)$	-3.5, -3.0, -2.5, -2.0, -1.5, -1.0
$\log(Z/Z_{\odot})$	-2, -1.5, -1, -0.5, 0.0, 0.5
Solar abundance set	Grevesse et al. (2010) solar abundance set
$\log(n_{\text{H}}/\text{cm}^{-3})$	8, 9, 10, 11, 12
Geometry	Plane-parallel; $\log(N_{\text{H}}/\text{cm}^{-2}) = 21 - 25$
Turbulence $v_{\text{turb}}/(\text{km/s})$	100, 200, 300, 400, 500, 600
Dust	No dust and no depletion onto dust

α_{ox} . We varied the ionization parameter, U , defined as the dimensionless ratio between the flux of the hydrogen ionizing photons and the hydrogen density, from -3.5 to -1.0 . We varied the overall chemical abundances from 1% of solar values to three times solar values, assuming the Grevesse et al. (2010) solar abundance set². The hydrogen density covers a range from 10^8 cm^{-3} to 10^{12} cm^{-3} , and the hydrogen column density ranges from 10^{21} cm^{-2} to 10^{25} cm^{-2} . These values are typical of the BLR clouds or their vicinity, and are those that can provide significant Fe II emission. According to Baldwin et al. (2004), a microturbulence velocity $> 100 \text{ km/s}$ is usually needed to describe the Fe II emission in AGNs. The main role of microturbulence is to increase the escape fraction of line photons and increase the strength of continuum pumping, which can increase the equivalent width (EW) of the Fe II emission and smooth the Fe II pseudo-continuum. We considered a broad range for the microturbulence velocity from 100 km/s to 600 km/s possible for the BLR in GN-z11 (Bottorff et al. 2000; Maiolino et al. 2024b). Finally, we assume the Fe II emitting region to lie within the dust sublimation radius and thus has no dust. We discuss the effects of different model parameters in Section 7.

To evaluate the effect of different components, we performed two sets of fits. In the first set, we only considered a power-law component and a Balmer continuum. In the second set, we added the Fe II emission. When fitting the continua, we exclude spectral regions with major emission lines. We note that the unresolved higher order Balmer lines would reach an intensity similar to the Balmer edge at 3646 \AA , making the Balmer jump hardly visible at 3646 \AA (Wills et al. 1985). Therefore, the strength of the Balmer jump is jointly constrained by the spectral regions at $\lambda \lesssim 3646 \text{ \AA}$ and $\lambda \gtrsim 3800 \text{ \AA}$, rather than by the region at $\lambda \approx 3646 \text{ \AA}$ only. We also note that we did not fit the stellar continuum in GN-z11 separately. The JWST/NIRCam images of GN-z11 show both an extended component and a compact central component, where the extended component contributes $\sim 1/3$ of the total fluxes in the rest-frame UV bands (Tacchella et al. 2023b). This puts an upper limit on the stellar contribution, given that part of the extended emission is likely outside the slit (and not accounted for by the slit losses). Even if we consider the contribution from the starlight separately, the Balmer break from young stellar populations in GN-z11 are negligible and should not impact the strength of the observed Balmer jump (see discussion and stellar SED decompositions in Tacchella et al. 2023b; Maiolino et al. 2024b)³.

² Although the abundance pattern in GN-z11 is likely different from the solar abundance pattern (Cameron et al. 2023b), we found the most important elemental abundance in our models is the relative abundance of Fe.

³ Also, in the case of the presence of both a Balmer jump and a Balmer break, one expects a dip at a wavelength slightly higher than 3646 \AA , because

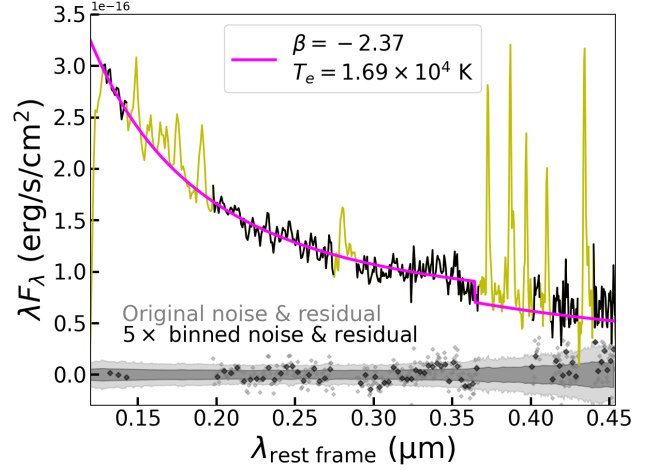


Figure 2. Best-fit model of the observed continuum of GN-z11 assuming a power-law function combined with an optically thin Balmer continuum (magenta). We only used the black part of the spectrum during the fit while excluding the yellow part due to the presence of prominent emission lines. The grey diamonds represent the residuals. The grey shaded region shows the 1σ uncertainty of the spectrum. The black diamonds and the black shaded region are the residuals obtained by rebinning every 5 pixels and the similarly rebinned uncertainty, respectively. The Balmer jump as shown by the model is offset from the jump in the continuum excess and the model does not reproduce the flattening of the continuum in the continuum excess region.

4 CONSTRAINTS ON THE BALMER CONTINUUM

To fit the continuum spectrum, we performed a Markov Chain Monte Carlo (MCMC) calculation using the PYTHON EMCEE package (Foreman-Mackey et al. 2013). We used the following likelihood function

$$\log L = \sum_{\lambda} -0.5(F_{\lambda}^{\text{PL}} + F_{\lambda}^{\text{BC}} - F_{\lambda})^2 / \sigma_{\lambda}^2. \quad (3)$$

In the equation above, F_{λ}^{PL} is a power-law function, F_{λ}^{BC} is a Balmer-continuum function, F_{λ} is the observed flux, and σ_{λ} is the uncertainty of the observed flux.

4.1 Optically thin Balmer continuum case

In the first fit, we assumed an optically thin Balmer continuum. During the fit, there are a total of three free parameters: the normalization of the power law, α , the power-law index, β , and the electron temperature, T_e . We assumed flat priors for these three

the Balmer break is not sharp due to the overlapping absorption from Balmer lines.

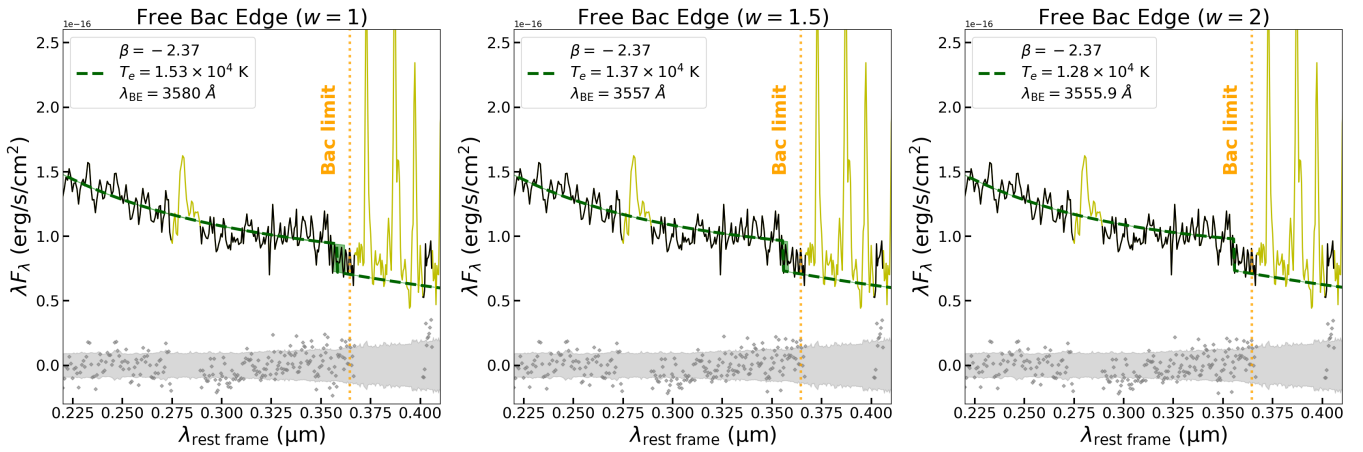


Figure 3. Best-fit model for the observed continuum of GN-z11 assuming a power-law function combined with an optically thin Balmer continuum with a free Balmer continuum edge. The continuum part of the observed spectrum is plotted in black and the part with emission lines is plotted in yellow. The dashed green line is the best-fit continuum model, with the shaded green region indicating the 1σ uncertainty of the location of the Balmer edge, λ_{BE} . The dotted orange line marks the location of the Balmer limit at 3646 Å. The grey diamonds and the grey shaded region represent the residuals of the fit and the 1σ uncertainty of the spectrum, respectively. From left to right, the contribution of the continuum excess region to the total χ^2 is re-weighted by a factor of 1, 1.5, and 2, respectively. Overall the blueshifted Balmer continuum models produce smaller residuals compared to the one that has a fixed Balmer edge, but the required blueshift is too large to be physical.

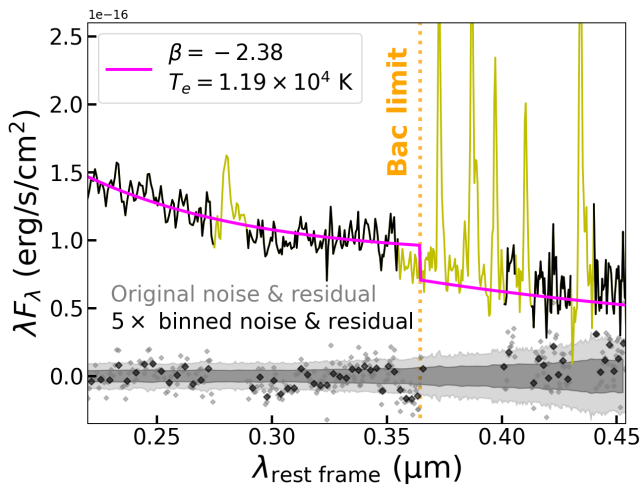


Figure 4. Best-fit model for the observed continuum of GN-z11 assuming a power-law function combined with an optically thin Balmer continuum. The continuum part of the spectrum is plotted in black and the part with emission lines is plotted in yellow. Different from Figure 2, the continuum region between 3550 Å and 3646 Å is masked during the fit. The solid magenta line is the best-fit continuum model. The dotted orange line marks the location of the Balmer limit at 3646 Å. The grey diamonds and the grey shaded region represent the residuals of the fit and the 1σ uncertainty of the spectrum, respectively. The black diamonds and the black shaded region are the residuals obtained by rebinning every 5 pixels and the similarly rebinned uncertainty, respectively.

parameters. We plotted our best-fit model in Figure 2, and list the model parameters as well as the corresponding 1σ uncertainties estimated from the posterior distributions in Table B1. The best-fit temperature is $T_e = 1.69^{+0.29}_{-0.23} \times 10^4$ K. We compared this Balmer continuum temperature, $T_e(\text{H}^+)$, with the temperature estimated from the auroral line $[\text{O III}]\lambda 4363$, $T_e(\text{O}^{2+})$. Since the JADES spectra of GN-z11 do not cover $[\text{O III}]\lambda 4959, 5007$, we used the empirical relations between $[\text{Ne III}]\lambda 3869/[\text{O II}]\lambda 3726, 3729$ and

$[\text{O III}]\lambda 5007/[\text{O II}]\lambda 3726, 3729$ fitted by Witstok et al. (2021) to estimate the flux of $[\text{O III}]\lambda 5007$ ⁴. The empirical relations were calibrated using star-forming (SF) galaxies and Seyferts from the Sloan Digital Sky Survey (SDSS, York et al. 2000). We thereby predicted the strengths of $[\text{O III}]\lambda 5007$ assuming an SF origin and a Seyfert origin separately. Then we estimated $[\text{O III}]\lambda 4363/[\text{O III}]\lambda 5007$, we used PYNEB (Luridiana et al. 2015) to compute the temperature at the low density limit as the lines we used mainly come from forbidden transitions of O^{2+} . The estimated temperatures are $T_e(\text{O}^{2+}) = 1.28^{+0.10}_{-0.12} \times 10^4$ K for an SF origin and $T_e(\text{O}^{2+}) = 1.33^{+0.11}_{-0.13} \times 10^4$ K for an AGN origin, which are consistent with the estimation of Cameron et al. (2023b).

Overall, $T_e(\text{H}^+)$ is higher than $T_e(\text{O}^{2+})$ by $\sim 1.5\sigma$, in contrast to the usual expectation that $T_e(\text{O}^{2+}) > T_e(\text{H}^+)$ due to the higher ionization potential of O^+ compared to H (Peimbert 1967). However, it is not much the temperature difference that is worrying, but the fact that the continuum excess region is not well fitted by the model. Indeed, the residuals clearly show a wiggling pattern near the jump. To make this issue more clear and to highlight its significance, in Figure 2, the residuals of the fit are rebinned and show clear deviations above and below the rebinned noise level at several locations within the continuum excess region.

A connected issue, is the fact that the continuum excess does not have a jump at the expected Balmer edge wavelength, but at shorter wavelengths. To check the significance of the shift, we set the location of the Balmer edge as another free parameter during the fit. The fitting result is shown in the left panel of Figure 3. The best-fit Balmer edge is at $\lambda_{\text{BE}} = 3580^{+40}_{-25}$ Å, which is 1.6σ shortward to the actual Balmer limit. However, the total χ^2 of the fit is not mainly driven by the continuum excess region, which tends to lower the significance of the mismatch of the Balmer jump. We found the posterior distribution of λ_{BE} has a peak around ~ 3550 Å and a tail towards longer wavelengths. Since we took the median

⁴ This approach is motivated by the observations that Ne/O remains roughly constant over a wide range of metallicities (Berg et al. 2020) and Ne^+ and O^+ have similar ionization potentials.

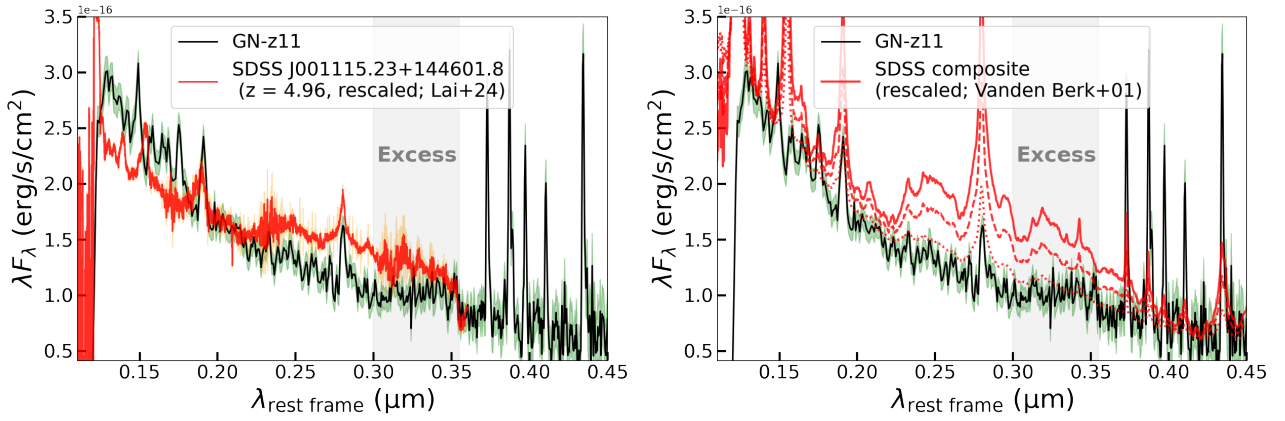


Figure 5. *Left:* comparison between the rest-frame spectrum of GN-z11 with that of a quasar at $z = 4.96$, SDSS J001115.23+144601.8, from the XQz5 catalog of [Lai et al. \(2024\)](#). The flux of the quasar spectrum is rescaled to compare with the GN-z11 spectrum. The green shaded region and the orange shaded region represent the 1σ uncertainties for the two spectra, respectively. The continuum excess region in GN-z11 is marked by the grey shaded region. *Right:* comparison between the rest-frame spectrum of GN-z11 with that of a modified composite spectrum constructed from 2200 quasars in SDSS by [Vanden Berk et al. \(2001\)](#). To better compare the nebular emission, the power-law continuum of the composite spectrum has been replaced with the power-law we fitted for GN-z11. The dotted, dashed, and solid red lines correspond to different scaling factors of the nebular emission. The grey shaded region marks the continuum excess identified in GN-z11.

of the posterior distribution as the best-fit value, the best-fit λ_{BE} is clearly shifted from the peak of the posterior distribution. If we simply increase the weight of the continuum excess by a factor of w during the fit, the fitting result becomes $\lambda_{\text{BE}} = 3557^{+23}_{-4}$ Å and $\lambda_{\text{BE}} = 3555.9^{+2.6}_{-3.7}$ Å for $w = 1.5$ and $w = 2$, respectively⁵. These fitting results are shown in the middle and the right panels of Figure 3. Overall, the main difference between the above fits is the location of the Balmer edge, which approaches ~ 3556 Å as the weight increases. Meanwhile, the rising or flattening feature of the continuum excess region is not captured by all models, resulting in overpredictions of the fluxes near 3000 Å.

Finally, we performed another test by masking the spectral region between the observed jump and the Balmer limit during the fit. The fitting result is shown in Figure 4. The residuals in the continuum excess region again show a wiggling pattern. This time, however, the model overpredicts the fluxes in the masked region of $3550 \text{ Å} < \lambda < 3646 \text{ Å}$ as expected.

Summarizing, a standard Balmer jump cannot reproduce the observed small blue bump excess seen in the spectrum of GN-z11.

4.2 Other possible scenarios involving the Balmer continuum

We also considered the possibility of a partially optically thick Balmer continuum. This model includes an additional free parameter, the optical depth at the Balmer edge, τ_{BC} . We discuss this case in Appendix B. Here we only summarize that the resulting fits (Figure B1) have a shape very similar to those with the optically thin case, and plagued by the same issues, with τ_{BC} being degenerate with the normalization of the continuum and temperature.

From the fits above, one can see the key feature that prevented a good fit with a Balmer continuum model is around the edge of the small blue bump. We also note that a potential trough centering at ~ 3480 Å (or an emission feature at ~ 3522 Å) and a potential emission

feature at ~ 3133 Å cannot be described by the simple continuum model. If we considered a scenario where a Balmer continuum did exist, the question becomes whether to trust a model with a strong jump but somehow blueshifted to around 3550 Å, or a model with a noise-limited weak jump where other emission features dominate the continuum excess.

For the strong-jump scenario, one needs a relatively low temperature and a small optical depth at fixed $F_{\text{H}\gamma}$. One might wonder whether a warm cloud in the foreground can absorb part of the Balmer continuum and create the blueshifted jump. Self-absorption of the Balmer emission is unlikely to produce a blueshifted Balmer jump. A potential source of absorption for the Balmer continuum is Fe^+ ([Wills et al. 1985](#)). However, there is a lack of Fe^+ lines between 3550 Å and 3646 Å. Also, one expects emission from Fe^+ rather than absorption in a typical BLR. Alternatively, one might speculate a blueshifted Balmer continuum in a warm outflowing cloud along the line of sight. There are two difficulties with this explanation. First, an ionized cloud with an outflow velocity of ~ 8000 km/s is required, but there are no blueshifted Balmer lines observed. Second, one expects high order Balmer lines to be blended with the Balmer jump especially given the spectral resolution of Prism⁶. Thus, there should be a smoothly declining edge rather than a sharp truncation even if the Balmer continuum is blueshifted.

4.3 The weak Balmer continuum scenario: a BLR origin

For the weak-jump scenario, the Balmer continuum becomes a secondary component and we need an alternative explanation for the continuum excess, which will be discussed in the next sections. If we simply exclude the spectral region between 3000 Å and 3550 Å (which we will associated with other emission features but keep the region between 3550 Å and 3646 Å to constrain the strength of the Balmer jump), then the solution is driven towards $T_e \sim 3 \times 10^4$ K, corresponding indeed to a strongly suppressed Balmer continuum.

⁵ If we only evaluate the χ^2 of the continuum excess region instead of using w , the result becomes $\lambda_{\text{BE}} = 3553 \pm 13$ Å. However, the power-law model as well as the temperature of the Balmer continuum would become poorly constrained.

⁶ The spectral resolution near the bump is $R \sim 280$ after taking into account the fact that the source is more compact with respect to the width of the shutter ([de Graaff et al. 2023](#)).

Such a high temperature averaged over H^+ is achievable if the ionized gas is either extremely metal-poor and/or the ionizing radiation field is hard enough. As a result, the temperature constraint under the weak-jump scenario provides another piece of evidence on the properties of the ionizing source in GN-z11. As we discuss in Section 8, compared to stellar radiation, ionization from an AGN is easier to achieve this temperature especially given the potentially enriched abundances in GN-z11. We will also discuss that such high temperature is completely inconsistent with the temperature inferred from the forbidden lines (tracing low density gas), in particular from the $[O\text{III}]\lambda 4363$ auroral line (which gives $T_e \sim 13,000$ K, as discussed above). The only solution in this case is that the bulk of the Balmer emission comes from the high density gas in the BLR, while the forbidden lines come from the narrow-line region (NLR) or the ISM of the host galaxy.

Alternatively, the Balmer continuum can be suppressed at a lower temperature but with a large optical depth. Both a high ionization parameter and a high density are needed to strongly obscure the Balmer edge. In fact, our CLOUDY models show to produce a similar suppression of the Balmer edge at $T_e \lesssim 20,000$ K to the optically thin case at $T_e \approx 30,000$ K, it is critical to have $n \gtrsim 10^6 \text{ cm}^{-3}$, which is atypical for an ISM origin. Therefore, to produce a suppressed partially optically thick Balmer continuum, one still needs a BLR with AGN ionization.

5 O III BOWEN FLUORESCENCE

With a weak jump, the next question is the identity of the emission that dominates the small blue bump. It is noteworthy that this continuum excess region is usually lack of strong emission lines. In this wavelength regime, AGNs can show the coronal line $[\text{Ne V}]\lambda 3426$ and the Bowen fluorescence line $\text{O III}\lambda 3133$ (Bowen 1934). There is, however, no detection of $[\text{Ne V}]\lambda 3426$. In contrast, there is potential detection of $\text{O III}\lambda 3133$ at a significance of 3.2σ . The resulting flux for this emission feature is $8.8 \pm 2.7 \times 10^{-20} \text{ erg/s/cm}^{-2}$.

We note that detection of $\text{O III}\lambda 3133$ was also reported recently for a JWST observed target at $z = 12.34$, GHZ2/GLASS-z12 (Castellano et al. 2024). As we show in Section 7, a redshifted Fe II bump can also produce the observed emission at 3133 \AA . We further discuss the implication of the emission at 3133 \AA in Section 8.

However, we note that the potential O III fluorescence can only account for one of the features seen in the hump.

6 INCONSISTENCY WITH THE WOLF-RAYET SCENARIO

Previously, it was also suspected that Wolf-Rayet (WR) stars could be present in GN-z11 and contribute to the chemical enrichment through their powerful winds (Cameron et al. 2023b; Senchyna et al. 2023). One might wonder whether the emission typically associated with winds from WR stars can produce the continuum excess we see in GN-z11.

It is known that nitrogen sequence WR (WN) stars can show strong nitrogen emission lines in the rest-frame UV (Abbott & Conti 1987). In the wavelength range of $3000 \text{ \AA} < \lambda < 3550 \text{ \AA}$, the strongest emission feature in WN stars is usually $\text{N IV}\lambda\lambda 3478, 3483$ (Garmanly et al. 1984; Conti & Massey 1989). However, at the expected location of this emission line ($\sim 3480 \text{ \AA}$), there is actually a trough in the continuum excess region in GN-z11. Thus, it is unlikely that the small blue bump is caused by WN emission.

In addition, as discussed by Maiolino et al. (2024b), the absence of

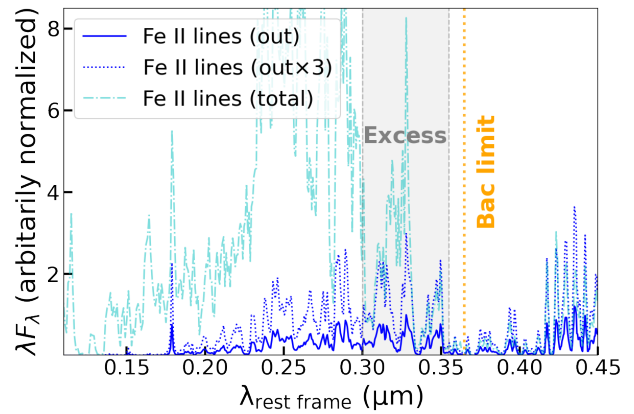


Figure 6. Example of an Fe II pseudo-continuum computed with CLOUDY. The total Fe II emission produced by the simulation is plotted as the dashed-dotted cyan line, and the Fe II emission propagated outwards is plotted as the solid blue line. The difference between the two sets of Fe II emission originates from the wavelength-dependent line optical depth, which leads to a more significant reduction of Fe II emission at $\lambda_{\text{rest frame}} < 3000 \text{ \AA}$. The dotted blue line was obtained by simply scaling up the flux of the outwards Fe II emission by a factor of 3. The grey shaded region indicates the continuum excess region identified in GN-z11. The dotted orange line marks the location of the Balmer limit.

$\text{N IV}\lambda 1718$ in GN-z11, which would be strong in WN stars showing strong $\text{N IV}\lambda 1486$, further argues against the presence of WR stars.

7 Fe II EMISSION

In a typical BLR, due to the high gas density and the destruction of dust grains, Fe^+ can be abundant and produce strong permitted emission lines in the UV. The resulting Fe II emission has been considered as the major contributor to the small blue bumps in quasar spectra. In Figure 5, we make a direct comparison between the spectrum of GN-z11 and quasar spectra at lower redshifts. In the left panel, we show the spectrum from a luminous quasar at $z = 4.96$ from Lai et al. (2024), where the small blue bump is apparent between 2000 \AA and 3550 \AA . Intriguingly, the small blue bump in the quasar shows a truncation just at 3550 \AA , similar to the truncation of the continuum excess in GN-z11. This truncation of the small blue bump traces the red end of the UV Fe II complex and is included in empirical UV Fe II templates for quasars (Mejía-Restrepo et al. 2016). The strength of the Fe II emission, however, varies strongly among quasars and the underlying physics remains poorly understood due to the complex production mechanisms and radiative transfer of Fe II lines (see e.g., Baldwin et al. 2004; Ferland et al. 2009; Gaskell et al. 2022, and references therein).

In the right panel of Figure 5, we show another comparison between an average quasar spectrum constructed by Vanden Berk et al. (2001) and the spectrum of GN-z11. The composite quasar spectrum of Vanden Berk et al. (2001) has a relatively strong and flat continuum. To better compare the jump feature, we replaced the continuum of the composite spectrum with that of GN-z11 and rescaled the strength of the nebular emission. The bump between 3000 \AA and 3550 \AA is clearly visible in the composite quasar spectrum, although the continuum excess bluewards of the small blue bump is stronger. The Fe II jump at $\sim 3550 \text{ \AA}$ is also present, and there is an additional jump likely caused by a Balmer continuum around 3800 \AA . In Appendix C, we provide a few other examples of Fe II jumps in ob-

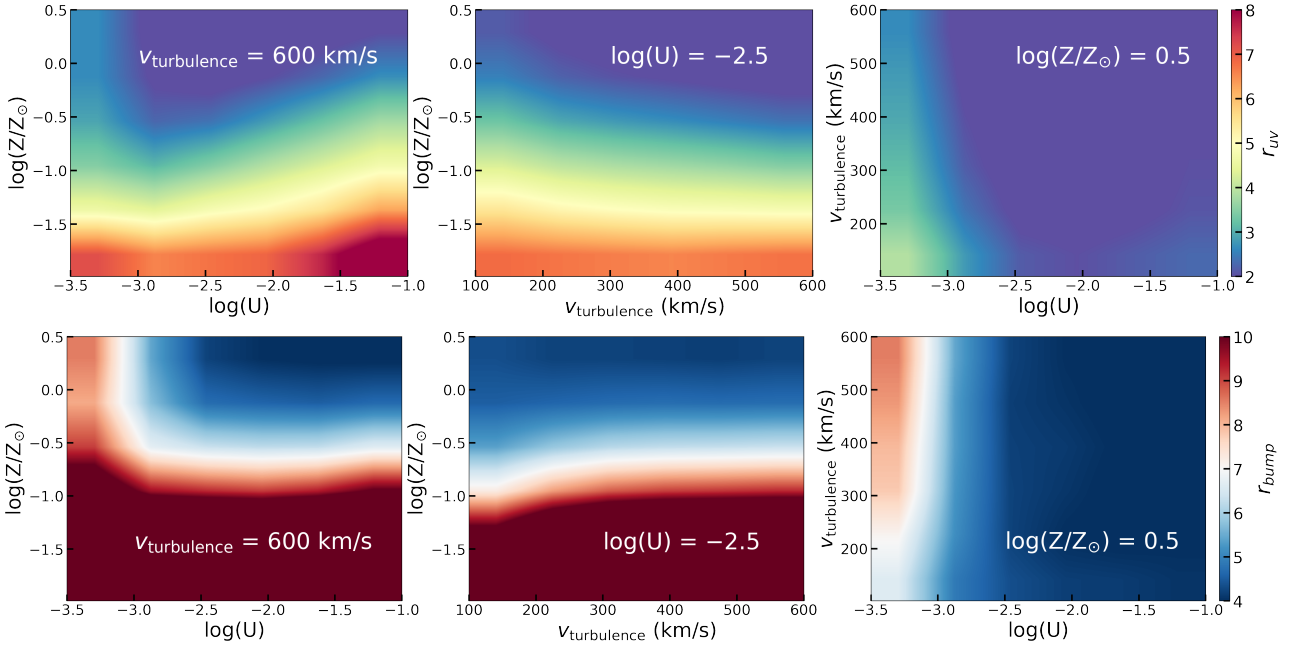


Figure 7. *Top:* the relative strength of the continuum excess, r_{uv} , as functions of the metallicity, ionization parameter, and turbulent velocity. In each panel, we varied two of the three parameters while keeping the third parameter at the value producing the smallest r_{uv} within the range of the parameter space (as shown by the white text in each panel). *Bottom:* the relative strength of the Fe II emission near the jump, r_{bump} , as functions of the metallicity, ionization parameter, and turbulent velocity. Definitions of r_{uv} and r_{bump} are given by Equations 4 and 5.

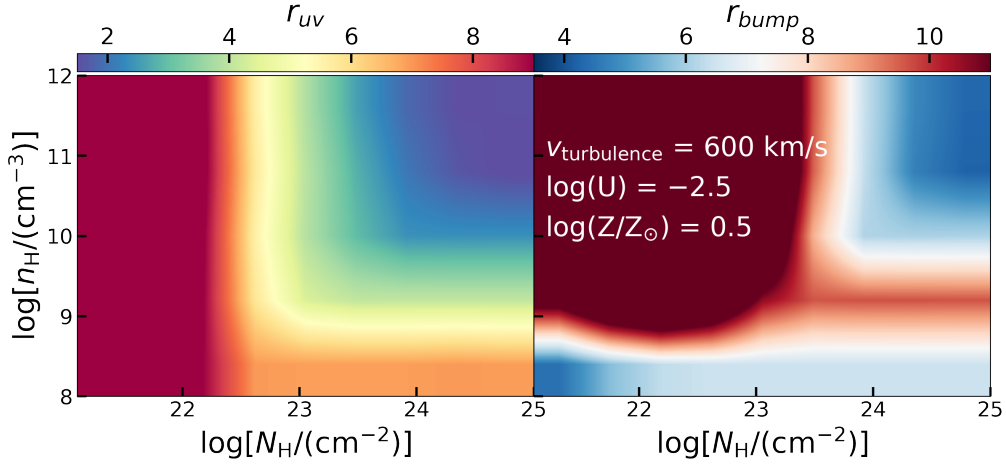


Figure 8. *Left:* the relative strength of the continuum excess, r_{uv} , as a function of the hydrogen volume density and the hydrogen column density. *Right:* the relative strength of the Fe II emission near the jump, r_{bump} , as a function of the hydrogen volume density and the hydrogen column density. The metallicity, ionization parameter, and turbulent velocity were fixed at the values producing the smallest r_{uv} within the range of the parameter space. Definitions of r_{uv} and r_{bump} are given by Equations 4 and 5.

servations of individual quasar spectra. A group of Fe II fluorescent lines around 3533 \AA is likely responsible for the Fe II jump (Netzer & Wills 1983), although the observed jumps in quasars all appear slightly redshifted to 3550 \AA .

The apparent difficulty associated with the Fe II explanation for the continuum excess is the atypical shape observed in GN-z11. In Figure 5, it is clear that Fe II emissions in both quasar spectra have higher fluxes at shorter wavelengths within the continuum excess region. In GN-z11, the “Fe II complex” is stronger towards the red end instead. One might wonder whether significant internal dust attenuation beyond the dust sublimation radius could produce this

shape. While the Balmer decrement is consistent with Case B values, it is possible that the Fe II emission originates from a different ionized region that has dust in the foreground (Shields et al. 2010). However, without an independent way to constrain the dust geometry, this approach gives too much freedom to Fe II models and the resulting optical Fe II emission might become too strong compared to UV Fe II emission. On the other hand, given that the physical conditions in GN-z11 are very different from lower-redshift quasars, we considered the possibility of producing a strong Fe II jump by exploring a large grid of dust-less CLOUDY photoionization models.

Table 1 summarizes the range of parameters we adopted for the

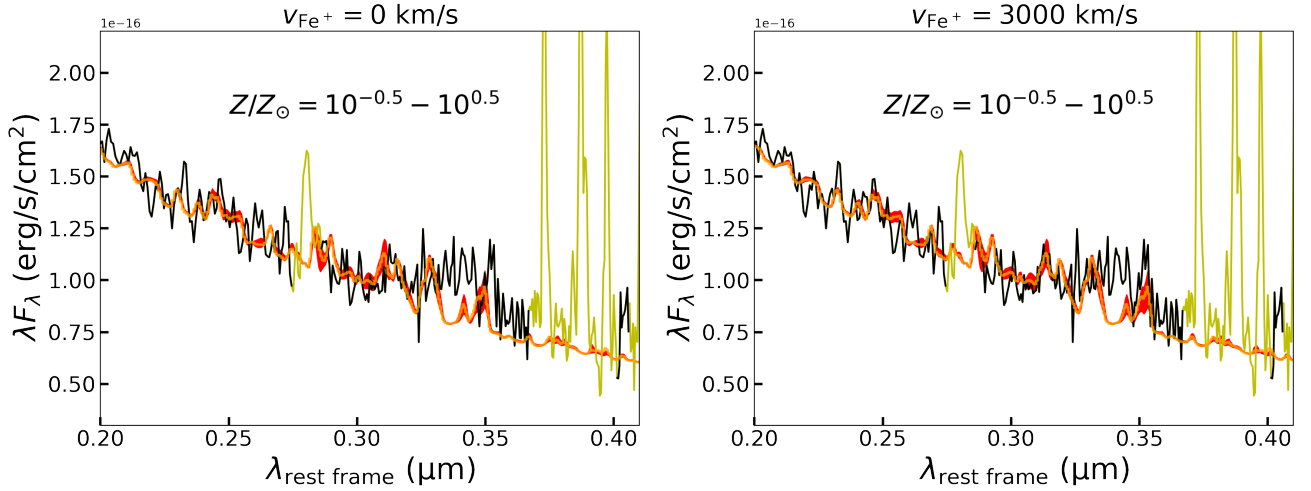


Figure 9. Comparisons between theoretical Fe II models with the observed bump in GN-z11. In each panel, the orange solid line represents an Fe II model with a solar metallicity combined with a power-law continuum model. The red shaded region shows the variation of the Fe II model within a range of metallicities from roughly 1/3 the solar value to 3 times the solar value (while keeping the normalization of the Fe II model the same). The solid black and yellow line is the Prism spectrum of GN-z11 in the rest frame. We only compared the black part of the spectrum with models. In the left panel, the relative velocity between the Fe II emitting clouds and the forbidden-line emitting clouds, v_{Fe^+} , is set to 0. In the right panel, however, v_{Fe^+} is set to 3000 km/s so that the Fe II emission is associated with a fast inflow within the BLR.

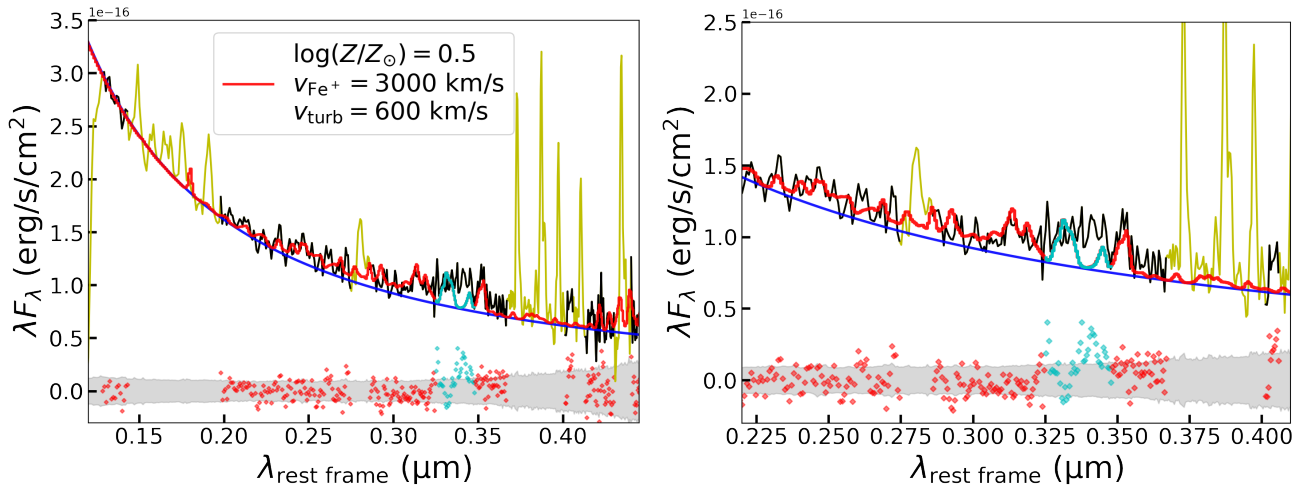


Figure 10. Comparisons between the theoretical Fe II model that has the strongest UV jump with the observed bump in GN-z11. The solid black and yellow line represents the Prism spectrum of GN-z11, where the black part is compared to the Fe II model. The solid red and cyan line is the Fe II model combined with a power-law model (the solid blue line). The part of the model that poorly matches the observed bump is colored in cyan. The relative velocity between the Fe II emitting clouds and the forbidden-line emitting clouds, v_{Fe^+} , is set to 3000 km/s. The grey shaded region indicates the 1σ uncertainty of the observed flux. The red and cyan diamonds are the differences between the observed spectrum and the Fe II model. The left panel shows the comparison over the full spectral range. The right panel is a zoom-in view around the bump.

Fe II models. We adopted a standard AGN SED for the ionizing source and a range of ionization parameters typically found in AGN ionized gas. For the metallicity, although the estimated oxygen abundance is around 1/10 the solar value based on forbidden lines (Bunker et al. 2023b), we considered metallicities up to super-solar values to take into account potential early enrichment of metals in the central region of GN-z11 (Cameron et al. 2023a; Maiolino et al. 2023b), where the Fe II emission originates. To allow strong permitted transitions of Fe⁺, it is necessary to have high densities, and thus we set $n_{\text{H}} \geq 10^8 \text{ cm}^{-3}$. In addition, we assumed the gas to be density-bounded as expected for typical BLRs and set the stopping column density, N_{H} , to range from 10^{21} cm^{-2} to 10^{25} cm^{-2} . Although a

hydrogen column density as high as 10^{25} cm^{-2} is atypical for low- z AGNs, such a value might not be uncommon for high- z AGNs that show BLR components in emission lines but lack X-ray emission (Maiolino et al. 2023b). A high column density combined with a high ionization parameter generally boosts Fe II emission due to the extended warm ionized zone with Fe⁺. Finally, the microturbulence velocity is an important parameter that changes the strength and shape of the Fe II emission (e.g., Netzer & Wills 1983; Verner et al. 1999). We allowed the microturbulence velocity to vary from 100 km/s to 600 km/s, encompassing the potential range of gas velocity dispersion in the BLR of GN-z11 probed by N IV]λ1486 ($\sigma = 200 \pm 21$ km/s) and He II λ1640 ($\sigma = 510 \pm 160$ km/s).

A key mechanism that can produce a strong Fe II jump at ~ 3550 Å relative to the Fe II emission bluewards to 3000 Å is the strong dependence of the Fe II optical depth on the wavelength. This generally leads to a greater reduction of the Fe II emission in the shorter wavelength in the emergent spectrum (Ferland et al. 2009). Figure 6 shows an example of an Fe II model with $\log(U) = -2.5$, $Z = Z_{\odot}$, $n_{\text{H}} = 10^{11} \text{ cm}^{-3}$, $N_{\text{H}} = 10^{25} \text{ cm}^{-2}$, and $v_{\text{turb}} = 500 \text{ km/s}$. While the total Fe II emission peaks around 2500 Å in the UV, the emergent Fe II emission is stronger in the continuum excess region of GN-z11. Between 3000 Å and 3550 Å, there are three groups of Fe II emission separated by two gaps in the emergent spectrum, with the rightmost one producing a jump close to the edge of the continuum excess region. We discuss below how flexible the shape of the UV Fe II emission is and whether the range of physical parameters preferred by the observed data is physically plausible.

7.1 Parametrization of the shape of the Fe II emission

To characterize the shape of the Fe II complex, we defined two parameters. The first parameter, r_{uv} , is defined as

$$r_{\text{uv}} \equiv F_{2000 \text{ Å} < \lambda < 3000 \text{ Å}} / F_{3000 \text{ Å} < \lambda < 3550 \text{ Å}}, \quad (4)$$

which describes the relative strength of the Fe II pseudo-continuum in the continuum excess region with respect to the part at shorter wavelengths. The second parameter, r_{bump} , is defined as

$$r_{\text{bump}} \equiv F_{3000 \text{ Å} < \lambda < 3550 \text{ Å}} / F_{3400 \text{ Å} < \lambda < 3550 \text{ Å}}, \quad (5)$$

which describes the relative strength of the Fe II emission making up the jump compared to the whole Fe II emission in the continuum excess region. As an example, for the model in Figure 6, $r_{\text{uv}} = 1.7$ and $r_{\text{bump}} = 4.2$ for the outwards Fe II emission, and $r_{\text{uv}} = 6.2$ and $r_{\text{bump}} = 8.6$ for the total Fe II emission. Given the shape of the observed continuum excess in GN-z11, we looked for models with both *small* r_{uv} and *small* r_{bump} .

To investigate the effect of different parameters, we started with a fiducial set of parameters typical for a Compton-thick BLR with $n_{\text{H}} = 10^{11} \text{ cm}^{-3}$ and $N_{\text{H}} = 10^{25} \text{ cm}^{-2}$, and varied the other three parameters, which are the metallicity, ionization parameter, and turbulent velocity. While the total hydrogen column density we adopted is much higher than what is usually adopted for lower redshift AGNs (with $N_{\text{H}} \sim 10^{23} \text{ cm}^{-2}$), it is not unexpected for high-redshift AGNs that show BLR components but are undetected in X-ray (Maiolino et al. 2023b; Maiolino et al. in prep). Within the range of the parameter space we considered, the minimum r_{uv} was found at $\log(U) = -2.5$, $\log(Z/Z_{\odot}) = 0.5$, and $v_{\text{turb}} = 600 \text{ km/s}$, and the minimum r_{bump} was found at $\log(U) = -1.0$, $\log(Z/Z_{\odot}) = 0.5$, and $v_{\text{turb}} = 300 \text{ km/s}$. While the values of $\log(U)$ and v_{turb} are possible for a highly ionized and turbulent BLR (or one having shears/velocity gradients on small scales; Bottorff et al. 2000), a super-solar metallicity seems too high for a galaxy $\sim 430 \text{ Myr}$ after the Big Bang and is in conflict with the sub-solar oxygen abundance inferred from forbidden lines (Bunker et al. 2023b). Still, based on different model assumptions, the potential range of the metallicity for GN-z11 could reach near-solar or even super-solar values (Cameron et al. 2023b; Isobe et al. 2023), especially in the very small region of the BLR (Maiolino et al. 2024b). We also note that the iron abundance is more important than the overall chemical abundances in these models, meaning a super-solar Fe/H combined with a sub-solar metallicity can reproduce these results as well.

Figure 7 shows the impact of different input parameters on the predicted r_{uv} and r_{bump} . We fixed one parameter at the value that produces the minimum r_{uv} or r_{bump} , and varied two remaining param-

eters at a time. The result shows that a metallicity of $\log(Z/Z_{\odot}) \gtrsim -0.5$ is critical to suppress the UV Fe II emission bluewards to the jump while enhancing the apparent jump strength. Meanwhile, an intermediate value of $\log(U)$ and a turbulent velocity of $v_{\text{turb}} \gtrsim 200 \text{ km/s}$ help to achieve the minimum r_{uv} and r_{bump} . The required turbulent velocity is compatible with the BLR velocity dispersion constrained by the width of N IV] $\lambda 1486$ and He II $\lambda 1640$ (Maiolino et al. 2024b). To check whether our choice of $n_{\text{H}} = 10^{11} \text{ cm}^{-3}$ and $N_{\text{H}} = 10^{25} \text{ cm}^{-2}$ significantly affect the determinations of minimum r_{uv} and r_{bump} , we further varied n_{H} and N_{H} over a larger range while keeping $\log(U)$, $\log(Z/Z_{\odot})$, and v_{turb} at values producing the minimum r_{uv} . Figure 8 shows the results of varying n_{H} and N_{H} . To minimize r_{uv} , one needs $n_{\text{H}} \gtrsim 10^{10} \text{ cm}^{-3}$ and $N_{\text{H}} \gtrsim 10^{24} \text{ cm}^{-2}$. For r_{bump} , while the global minimum is at $n_{\text{H}} = 10^8 \text{ cm}^{-3}$ and $N_{\text{H}} = 10^{21} \text{ cm}^{-2}$, combined with the constraints from r_{uv} , one still needs $n_{\text{H}} > 10^{10} \text{ cm}^{-3}$ and $N_{\text{H}} > 10^{24} \text{ cm}^{-2}$. The latter implies Compton-thickness, typical of other high-redshift AGNs (Brightman & Ueda 2012; Lanzuisi et al. 2018). The large n_{H} is typical of the BLR clouds. Finally, the high metallicity is also typical of the BLR of AGN, although at such early epochs the very high Fe enrichment might be puzzling, but as much as the high nitrogen enrichment has been puzzling for this and other high- z galaxies (Cameron et al. 2023b; Isobe et al. 2023; Senchyna et al. 2023; Topping et al. 2024). We discuss this point in detail in Section 8.

Issues however remain even if we adopt high-metallicity models. The minimum values of parameters predicted by the models are $r_{\text{uv}} = 1.5$ and $r_{\text{bump}} = 3.9$. If we fit a power-law to the observed spectrum while excluding the bump region, and took the residual as the potential Fe II emission, the corresponding r_{uv} is basically noise-limited and $r_{\text{bump}} = 1.1 \pm 0.2$, which are significantly smaller than the model predictions. The differences are in part due to the gaps between groups of Fe II emission in the wavelength space, which are not observed in typical quasar spectra as well as in GN-z11. The absence of the gaps could be a result of broadening by the line spread function (LSF) of the instrument, broadening by the intrinsic velocity dispersion of the BLR, and pumping of unaccounted transitions by nearby lines and continua (Netzer & Wills 1983; Verner et al. 1999; Baldwin et al. 2004; Ferland et al. 2009; Sarkar et al. 2021). Next, we directly compared the models with the bump in GN-z11 taking into account the above effects.

7.2 Comparison with the observed bump

In Figure 9, we compare three sets of Fe II models with $\log(Z/Z_{\odot}) = -0.5, 0$, and 0.5 combined with a power-law continuum model to the observed spectrum of GN-z11. Based on the analysis in the previous subsection, we set $\log(U) = -2.5$, $v_{\text{turb}} = 600 \text{ km/s}$, $n_{\text{H}} = 10^{11} \text{ cm}^{-3}$, and $N_{\text{H}} = 10^{25} \text{ cm}^{-2}$ for these models. We set the normalization of the Fe II emission as a free parameter to take into account the possibility that it arises from a region different from other strong lines in the BLR (e.g., Ferland et al. 2009) and adopted the normalization that best reproduces the small blue bump. Before we made the comparisons, we broadened the Fe II models by an LSF constructed from combining the broadening by the microturbulence in the models and the broadening by the instrumental resolution ($\sim 1.1 \times 10^3 \text{ km/s}$).

Finally, judging from Figures 5 and 6, the theoretical Fe II jump generated by CLOUDY is slightly blueshifted compared to the observed jump, meaning the Fe II emission in GN-z11, if it exists, should be redshifted with respect to other strong emission lines. In fact, Fe II emission was often found to be redshifted in quasar spectra

at lower redshifts and redshift velocities up to 3000 km/s were reported previously (Hu et al. 2008a,b). As an example, in Figures 5 and C1, the Fe II jumps in these quasars are not significantly blueshifted with respect to the jump seen in GN-z11. We therefore performed a separate comparison using redshifted Fe II models in the right panel of Figure 9, and further discuss its physical explanation in Section 8.

While compared to the Balmer continuum models in Figure 2, the Fe II models fail to reproduce the middle part of the small blue bump due to the aforementioned gaps between different groups of Fe II emission, the Fe II models are able to recover certain observed features near the boundaries of the bump. One can see clear Fe II jumps in the models, which match the observed jump increasingly better with increasing metallicity, especially for those models having a velocity shift of ~ 3000 km/s. On the other hand, the potential emission line at 3133 Å can be explained by a group of redshifted Fe II emission, as shown in the right panel of Figure 9. In Figure 10, we compare the highest metallicity Fe II model that produces the strongest UV jump with the observed bump in GN-z11. While the Fe II jump in the model well resembles the observed jump at 3550 Å, the flux of the observed bump between 3300 Å to 3480 Å is clearly underestimated by the model.

The question now becomes whether it is possible to fill the gaps between the Fe II emission. In Figure 5, the Fe II emission in quasars does not exhibit noticeable gaps in the continuum excess region. If the absence of gaps is purely due to the broadening of Fe II line profiles, one needs an intrinsic FWHM $\geq 8 \times 10^3$ km/s. Although with a larger microturbulence velocity, the Fe II emission in the continuum excess region would become even stronger with respect to the Fe II emission at shorter wavelengths (and thus produce a stronger bump), the required broadening is significantly larger than the measured widths of semi-forbidden lines and permitted lines in GN-z11, which presumably come from the same BLR that produces the Fe II emission.

Alternatively, one might wonder whether any unaccounted line/continuum fluorescence of the Fe II emission between the gaps could explain the model mismatch. Indeed, from the observed high-resolution quasar spectra as well as the empirical Fe II templates constructed from them, the gaps we see in the models are also filled with lines (e.g., Tsuzuki et al. 2006; Mejía-Restrepo et al. 2016). Thus, it is possible that our current models still do not fully capture the fluorescence of the Fe II emission between 3000 Å and 3550 Å. A full scrutiny of the physical processes in Fe II modeling is beyond the scope of this work and we leave the theoretical calculation of the Fe II emission under extreme physical conditions for future investigations. In what follows, we simply consider the Fe II emission as a candidate to produce the jump feature while discussing the physical interpretations.

8 DISCUSSION

In the previous sections we have attempted fitting the observed continuum in the Prism spectrum of GN-z11 using combinations of a power-law model, a Balmer continuum model, and Fe II emission models. Although none of the models is able to fully reproduce the small blue bump in GN-z11, the preferred ranges of the model parameters and the failure of a good fit itself indicate an uncommon origin of the small blue bump. In this section, we discuss the implications of our results.

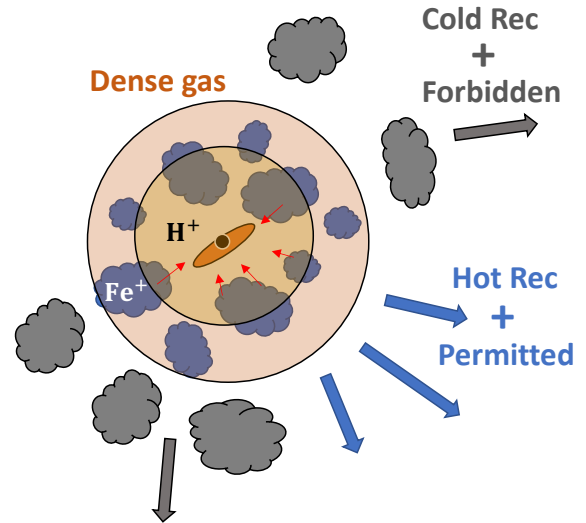


Figure 11. Schematic plot illustrating the inferred ionization structure within the nuclear region of GN-z11. In the central BLR that hosts dense gas clouds, Balmer recombination emission including continua and lines comes from the inner and hot region. In contrast, permitted emission of Fe II mainly comes from partially ionized region at large column densities, where the clouds might be infalling. Finally, outside the BLR and in the rest of the galaxy, there is also Balmer recombination emission from low density gas with lower temperatures, which is co-spatial with forbidden lines of metals. The plot does not reflect the actual physical scales of different regions.

8.1 Presence of different ionized regions

8.1.1 Hot gas with hydrogen Balmer emission

As shown by Maiolino et al. (2024b), gas clouds with different densities are likely present in GN-z11. On the one hand, constraints from the semi-forbidden $N\text{IV}] \lambda 1486$ relative to $[N\text{IV}] \lambda 1483$, and the relative strengths of the semi-forbidden $N\text{III}]$ multiplet indicate these UV emission lines to originate from high density clouds with $n_{\text{H}} \geq 10^9 \text{ cm}^{-3}$, consistent with BLR clouds. On the other hand, the presence of strong, forbidden $[O\text{III}] \lambda 4363$ requires densities much lower than the UV-line emitting clouds, and consistent with NLR (or simple ISM) clouds.

As we have shown, given the observed strength of $H\gamma$, if the Balmer-line emitting gas has a temperature similar to the $[O\text{III}]$ -line emitting gas, $T_e(O^{2+}) \approx 1.3 \times 10^4$ K, one expects a detectable Balmer jump clearly different from the shape of the continuum excess. If the continuum excess is dominated by some other mechanisms, which is our preferred solution, then the Balmer jump is weak enough that the best-fit temperature would be $T_e(H^+) \approx 3 \times 10^4$ K, implying the observed Balmer emission to originate from gas much hotter than the forbidden-line emitting gas.

We note that low-redshift observations of individual H II regions or Planetary nebulae frequently show $T_e(H^+) < T_e(O^{2+})$ (e.g., Peimbert 1967), clearly the opposite to what we found in GN-z11. In the low-redshift cases, the temperature difference potentially rises from micro-fluctuations of temperature or chemical abundance inhomogeneities within individual nebulae (Peimbert et al. 2017). In the case of GN-z11, however, we argue the temperature difference is created by the spatial distributions of gas clouds responsible for different emission lines.

The observed Balmer emission can have two components, one

from hot and dense gas close to the accretion disk (the BLR), and the other from less-dense and colder clouds at a larger distance from the accretion disk (the NLR or SF-ionized ISM). These two components are not separable kinematically due to the limited spectral resolution. The hot-dense component has a negligible Balmer jump due to its high temperature, and the Balmer jump in the cold and low-density component is weak simply because the flux of the cold component is subdominant. Forbidden lines such as [O III] λ 4363 are only present in the cold and low-density gas, together with the cold Balmer component, due to their low critical densities. One might wonder whether this explanation leads to an unphysically high [O III] λ 4363/H γ in the cold gas. Interestingly, high [O III] λ 4363/H γ values have been observed in a number high- z galaxies by JWST, especially AGNs (Übler et al. 2023a; Mazzolari et al. 2024), with a few galaxies even showing [O III] λ 4363/H γ \sim 1. A hard ionizing radiation from AGN combined with metal-poor gas can give rise to a high [O III] λ 4363/H γ in an NLR. For a rough estimation, if we simply use [O III] λ 4363/H γ < 1 to set a prior for the flux of the cold H γ , and fit the continuum assuming both a hot component and a cold component (whose temperature is fixed to 1.3×10^4 K), we obtain $H\gamma_{\text{cold}} = 0.43^{+0.24}_{-0.14} H\gamma_{\text{total}}$. This calculation also slightly lowers the temperature estimation for the hot component to $T_e = 2.6^{+0.4}_{-0.6} \times 10^4$ K.

We emphasize that for the hot component, a high density is necessary to explain the missing Balmer jump while avoiding overpredicting the strength of [O III] λ 4363. This requirement rules out the possibility of the hot component being the ionized gas within the low-density NLR or the ISM ionized by young stars. In addition, for the ISM ionized by young stars, it is difficult to reach a temperature of $T_e \sim 3 \times 10^4$ K. One might wonder whether the BLR can reach such a high temperature. Indeed, due to the high density of the gas and the absence of dust depletion, the cooling through metals within the BLR could be efficient. However, cooling in the BLR would be limited to semi-forbidden and permitted transitions due to the high density. With CLOUDY, we calculated volume-average electron temperatures in clouds ionized by young stellar populations and AGN, as shown in Figure D1. While SF models cannot produce high enough temperatures even if $\log(Z/Z_\odot) \sim -3$, both NLR and BLR models are able to reach $T_e(\text{H}^+) \sim 3 \times 10^4$ K at $\log(Z/Z_\odot) \sim -1$ and $\log(U) \sim -1$. The problem with the NLR model, however, is that the corresponding [O III] λ 4363 is too strong compared to what has been observed in GN-z11.

Another complicating factor for BLRs is the physical conditions for different emission line species can well be different as they are optimally emitted by different clouds (Baldwin et al. 1995). Again, we caution that when the Balmer edge become partially optically thick in the BLR, it can be suppressed at the same level but at a lower temperature (Grandi 1982). Regardless, the requirement for the gas to be dense remains the same, and the presence of an BLR is preferred given the little contribution of the Balmer continuum to the small blue bump.

Figure 11 shows our inferred ionization structure in the nuclear region of GN-z11. The BLR produces the continuum excess we see in the near-UV as well as permitted and semi-forbidden emission lines. The Balmer continuum originates in a hot and dense region within the BLR. In contrast, Fe II emission likely originates in a partially ionized zone with high column densities. Finally, forbidden lines and part of the Balmer lines in the optical come from a less dense and colder region in the NLR or the ISM. Although we propose the Balmer lines to have origins from different regions, they are kinematically indistinguishable, especially with the limited signal-to-noise of current observations. Indeed, the broadening of lines in the BLR of GN-z11 by virial motions is only on the order of a few hundred kilo-

meters per second due to its small black hole mass (Maiolino et al. 2024b). However, it may be possible to spatially resolve some of the NLR/ISM components with integral field spectroscopy, as illustrated in Maiolino et al. (2023a).

The presence of two Balmer components would also indicate biases in abundance estimations based on the assumption that the entire Balmer emission comes from the forbidden-line emitting clouds. Our estimated $H\gamma_{\text{cold}}$ corresponds to $[\text{O III}]\lambda 4363/H\gamma_{\text{cold}} \approx 0.53^{+0.33}_{-0.09}$, resulting in an abundance of $12 + \log(\text{O}/\text{H}) = 8.18^{+0.48}_{-0.27}$ assuming higher ionization states of oxygen are negligible. The uncertainties in the above value include uncertainties in the flux of $H\gamma_{\text{cold}}$ as well as uncertainties in the O^{2+} temperature. Although there is another uncertainty associated with converting the O^{2+} temperature to the O^+ temperature in the NLR, it is at the level of ~ 0.01 dex in our case assuming the temperature relations for AGNs in Dors et al. (2020). While our lower abundance estimation is broadly consistent with the value obtained by Cameron et al. (2023b), the fiducial value we obtained is about 30% of the solar value and is about two times the previously estimated value. High chemical abundances in high- z AGNs are commonly seen (Nagao et al. 2006a,b; Juarez et al. 2009; Matsuoka et al. 2009, 2011, 2018; Guo et al. 2020). We caution, however, that the range of the abundance we derived depends on the prior on the range of [O III] λ 4363/H γ_{cold} . A lowered upper limit for [O III] λ 4363/H γ_{cold} would produce an overall lower metallicity estimation. To settle this problem, it is vital to have high spectral resolution observations of Balmer lines, which are unfortunately missed due to the truncation of the high-resolution NIRSpect grating spectrum in the previous observation (Maiolino et al. 2024b).

8.1.2 Infalling gas with a high column density

As we show in the previous section, if Fe II emission is responsible for the observed bump in GN-z11, the gas with Fe II emission should be redshifted at a velocity of ~ 3000 km/s with respect to other line-emitting regions. Such a high velocity would indicate a fast inflow. As shown by Hu et al. (2008a,b), it is not uncommon for Fe II emission to be redshifted with respect to narrow emission lines and broad emission lines in quasars. Within a sample of 4037 quasars from SDSS (York et al. 2000) at $z < 0.8$ inspected by Hu et al. (2008b), the typical velocity shift of Fe II is ~ 400 km/s, and the largest velocity shift of Fe II clearly exceeds 2000 km/s and even reaches 3000 km/s.

To explain the ubiquitous shift in Fe II velocity, Ferland et al. (2009) proposed a scenario where Fe II emission comes from infalling clouds with large column densities viewed from their shielded faces, to which the gravitational pull overcomes radiation pressure from accreting supermassive black holes (SMBHs). In fact, for the SMBH in GN-z11 that is likely accreting at a super Eddington rate of $L/L_{\text{Edd}} \sim 5$ (Maiolino et al. 2024b), the required column density would be $7.5 \times 10^{24} \text{ cm}^{-2}$ according to the equation given by Ferland et al. (2009). The column density needed is in good agreement with the best-fit Fe II model we adopted.

Finally, the infalling Fe II emitting clouds should have a high Fe abundance as well to enhance the Fe II emission at $3000 \text{ \AA} < \lambda < 3550 \text{ \AA}$. An interesting question is whether the potentially enriched Fe is related to the ‘‘abundance anomaly’’ in GN-z11, where nitrogen appears particularly enriched compared to oxygen, which we discuss in the next subsection.

8.2 Revisiting the “abundance anomaly”

One of the most puzzling features in the spectrum of GN-z11 is the strong N IV] and N III] emission in the UV. Based on the high N III]/O III] in the UV, [Bunker et al. \(2023b\)](#) and [Cameron et al. \(2023b\)](#) derived a super-solar N/O, indicating a fast and/or exotic chemical enrichment in GN-z11. With the new evidence from the potential Fe II emission, it is possible that iron is also enriched in GN-z11. It is noteworthy that high Fe abundances were also found in nitrogen-loud quasars at lower redshifts and were predicted by chemical enrichment models of quasars (e.g., [Hamann & Ferland 1993](#)). In addition, recent JWST observations have revealed potential early enrichment of Fe as traced by forbidden transitions of Fe in a galaxy showing a prominent Balmer jump at $z = 5.94$ ([Cameron et al. 2023a](#); [Tacchella et al. 2024](#)), and in an AGN host galaxy at $z = 5.55$ ([Übler et al. 2023b](#); [Ji et al. 2024](#)). To explain the high N/O, [Maiolino et al. \(2024b\)](#) suggest a possibility that the UV emission mainly originates in the BLR of the AGN in GN-z11, making the fast chemical enrichment within such a small region ($\sim 10^{-2}$ pc) and small gas mass (a few solar masses) possible without invoking any exotic enrichment channels. Similarly, since the Fe II emission mainly comes from clouds in the BLR, a fast enrichment of Fe towards the solar value is also compatible with the scenario above.

In addition to the fast enrichment of the overall chemical abundances within a small region, it is possible to achieve high Fe/O at low metallicities, which would give rise to the a strong Fe II complex without invoking a high oxygen abundance. According to the models of [Vanni et al. \(2023\)](#), it is possible for high-mass Pair Instability Supernovae (PISNe) to produce super solar Fe/O even when Fe/H is as low as 1 – 10% the solar value. An early enrichment of Fe is also possible through ejecta from hypernovae (HNe), especially given a potentially dense star formation environment of GN-z11 ([Isobe et al. 2023](#); [Watanabe et al. 2024](#)). It is noteworthy that solar abundance ratios of Fe/O have also been observed in several extremely metal-poor galaxies in the local Universe and it is suspected that the enrichment of Fe is produced by PISNe, HNe, or SNe of supermassive stars with stellar masses of $M_* \gtrsim 300 M_\odot$ (e.g., [Kojima et al. 2021](#); [Isobe et al. 2022](#)). The production of supermassive stars, on the other hand, might come from the stellar encounters in the dense nuclear environment of GN-z11 as suggested previously for dense globular clusters (CGs; [Gieles et al. 2018](#)). In the local Universe, Fe is mainly enriched by Type-Ia SNe that has a typical delay time from 100 Myr to 1 Gyr. However, we note that the first Type-Ia SNe can occur only ~ 30 Myr after the initial star formation (see e.g., [Maiolino & Mannucci 2019](#), and references therein). According to the SED fitting of the JWST/NIRCam photometry of GN-z11 by [Tacchella et al. \(2023b\)](#), the extended part of the source has a SFH with a rising SFR starting from a look-back time of ~ 50 Myr, which then shows a peak of SFR at a look-back time of ~ 20 Myr. Therefore, it is still possible that the initial enrichment of Fe by Type-Ia SNe from the progenitors created in the rising phase of the past star formation starts to take effect at the time of observation. However, such a scenario would also require suppression of oxygen enrichment by previous core-collapse supernovae (CCSNe), or a dilution of the oxygen abundance, which might be achieved through inflow of pristine gas. Still, considering the mismatch between our photoionization models and data due to gaps in the models, it is important for future work to have more detailed modeling of the emission lines in the BLR in the early Universe.

Finally, a caveat of interpreting the strong high-ionization UV lines in GN-z11 as a sign of a high abundance is the optical-depth effect in BLRs. As the density and ionization parameter in an BLR become too high, the emission lines start to be dominated by a Black-body

component near the surface of the cloud and their ratios no longer reflect the actual chemical abundances ([Temple et al. 2021](#)). To check this effect, we computed a series of photoionization models for BLRs having a range of hydrogen densities and ionization parameters while adopting a low metallicity and N/O. We found at $\log(Z/Z_\odot) = -1$ and $\log(N/O) = -1.5$, both N III]/O III] and N IV]/O III] can be greater than one when $\log(U)$ reaches 0 and the surface emission starts to dominate. However, at such a high ionization parameter, N IV] would be significantly stronger than N III], which contradicts the similar fluxes of N IV] and N III] observed in GN-z11. Therefore, with a BLR origin for the UV nitrogen lines, we still need chemically enriched gas in order to match models with the observation.

8.3 Potential implications of the Bowen emission

While in the previous section, we fitted the emission feature detected at $\sim 3\sigma$ at 3133 Å with a redshifted peak within the UV Fe II complex, it is also possible that the emission feature is the Bowen fluorescence line, O III]3133. This line is produced via fluorescence of O III]303.8 with He II Ly α (i.e., Bowen fluorescence; [Bowen 1934](#)), and it is usually the strongest Bowen line of O III] in the near UV. Strong O III]3133 emission has been observed in AGNs, planetary nebulae (PNs), symbiotic stars ([Kastner & Bhatia 1996](#)), and more recently, in a galaxy at $z = 12.34$ ([Castellano et al. 2024](#)).

The strength of O III]3133 strongly depends on the fraction of He II Ly α photons that are resonantly absorbed by O III]303.8 and converted to Bowen emission, or the “Bowen efficiency” ([Kallman & McCray 1980](#)). Thus, the flux of the Bowen line is sensitive to the shape of the ionizing SED as well as the metallicity, which greatly impacts the resulting abundance ratio of He⁺⁺/O⁺⁺ in the ionized gas. The physical conditions of the BLR in GN-z11 could provide the environment that boosts the strength of the Bowen emission. According to the photoionization calculations by [Netzer et al. \(1985\)](#), in dense PNs or BLRs of AGNs, the flux of O III]3133 can be similar or even several times higher than that of He II 4686. While the JWST spectra of GN-z11 do not cover He II 4686, we can use the flux of He II 1640 to make a rough estimation. This is motivated by the fact that the flux ratio of He II 1640/He II 4686 is typically 7 – 8 in all kinds of nebulae. According to the measurements by [Maiolino et al. \(2024b\)](#), $F(\text{He II } 1640) = 6.0^{+1.4}_{-1.3} \times 10^{-19}$ erg/s/cm⁻². Our measured flux of the emission line at 3133 Å is $8.8 \pm 2.7 \times 10^{-20}$ erg/s/cm⁻², which is roughly 1/7 of the flux of He II 1640. Therefore, the strength of the Bowen emission line is likely similar to that of He II 4686 and is indeed what one would expect for a BLR origin.

To better understand the origin of this line, it is important to re-examine JWST-confirmed high- z Type-1 AGNs with strong He II 4686 emission. Also, it would be useful to compute photoionization models with physical conditions appropriate for AGNs in early galaxies. However, this is beyond the scope of the current paper, and we leave it for future investigations.

8.4 Is the small blue bump unique?

In previous sections, we discussed potential physical origins for the small blue bump in GN-z11. Specifically, we investigated the scenario where the bump is a blend of Fe II lines rather than part of a Balmer continuum. One might wonder whether there is other observational evidence of similar bumps in the spectra of early galaxies. Given the extreme physical conditions of GN-z11, it is possible that the small blue bump is a rare case. Interestingly, we did find another galaxy in JADES that show a very similar continuum excess in the UV. This

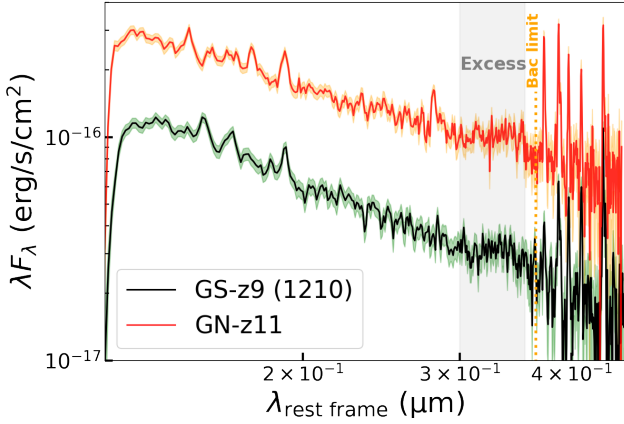


Figure 12. Comparison between the Prism spectrum of JADES-GS-z9-0 and that of GN-z11 on a log scale. The shaded regions correspond to the 1σ uncertainties of the spectra. The grey band marks the continuum excess region and the orange dotted line marks the location of the Balmer limit.

galaxy, JADES-GS+53.11243-27.77461, has a redshift of 9.433 and was observed in the GOODS South field (hereafter JADES-GS-z9-0) in both Cycle 1 Program 1210 (P.I.: N. Luetzgendorf; [Bunker et al. 2023a](#)) and Cycle 2 Program 3215 (P.I.: D. Eisenstein; [Eisenstein et al. 2023b](#)). Its nebular emission was analyzed by [Cameron et al. \(2023c\)](#), and it was later classified as a Type-2 AGN by [Scholtz et al. \(2023b\)](#) based on UV emission-line diagnostics and the presence of the high ionization line [Ne IV] λ 2422 (as well as the absence of broad emission lines), and more recently by Curti et al. in prep based on the detection of the coronal line [Ne V] λ 3426.

Figure 12 shows the Prism spectrum of JADES-GS-z9-0 from the Program 1210 along with the Prism spectrum of GN-z11. One can see a bump within the continuum excess region in JADES-GS-z9-0, whose shape, however, is different from that in GN-z11 and does not exhibit a sharp jump at ~ 3550 . While the bump in JADES-GS-z9-0 cannot be well described by a Balmer continuum, Fe II models cannot provide a good fit as well due to the smoothly declining edge of the bump.

Intriguingly, the small blue bump in JADES-GS-z9-0 disappears in the observation of the Program 3215. Figure 13 shows a comparison between the Prism spectrum in the Program 1210 and that in the Program 3215 for JADES-GS-z9-0. While the overall UV continuum rises in 3215 (as shown by the overall positive residuals), the UV slope slightly flattens. By fitting power-law functions to the UV continua of the two spectra, we obtained a slope of $\beta = -2.47 \pm 0.04$ for the 3215 spectrum when including the Balmer continuum, and $\beta = -2.35 \pm 0.03$ when excluding the Balmer continuum. In comparison, the UV slope of the 1210 spectrum is $\beta = -2.58 \pm 0.03$ if the bump region is excluded. We checked the shutter positions of the two observations and found the positioning is unlikely the cause to the difference of the UV flux. Also, the two Prism spectra were obtained with the same data reduction procedure.

In the rest frame of JADES-GS-z9-0, the two observations are separated by ~ 1 month and we speculate this systematic change in the UV is indicative of spectral variability in the AGN. While JADES-GS-z9-0 was a Type-2 AGN classified from the previous observations, we might be witnessing the rise of the underlying UV continuum from the AGN accretion disk, a process found in “changing-look quasars” in lower redshifts ([MacLeod et al. 2019](#)). The small blue bump either has responded to the change of the UV continuum in 3215, or is simply overwhelmed by the rising

continuum. According to the standard BLR model with a stratified ionization structure, emission from different ionic species respond to the continuum variability differently ([Ulrich et al. 1997](#)). Therefore, the variability of the small blue bump could provide clues on its origin, which requires follow-up observations of this target. In fact, the UV continuum of JADES-GS-z9-0 in 3215 appears more smooth and can be described by a power-law function and an optically thin Balmer continuum with $T_e = 2.0 \pm 0.5 \times 10^4$ K, as shown in Figure 13. The best-fit Balmer temperature is consistent with the temperature inferred from [O III] λ 4363 as well as the temperature inferred from O III] λ 1666 (Curti et al. in prep).

In summary, the Prism spectrum JADES-GS-z9-0 shows a small blue bump at a similar spectral location as that in GN-z11, although with a slightly different shape. The bump in JADES-GS-z9-0 seems to be linked to its potential spectral variability. Future observations of the UV spectrum of JADES-GS-z9-0 is needed to verify the variability and provide more evidence on the identify of the small blue bump.

9 CONCLUSIONS

In this work we investigated the physical origin of the continuum excess between 3000 Å and 3550 Å in the JWST/NIRSpec Prism spectrum of GN-z11. The continuum excess is significantly detected in the spectrum at 7.8σ and shows a sharp jump around 3550 Å. This excess in the UV partly resembles the shape of the small blue bump observed in typical quasar spectra, typically associated with Fe II complex emission from the Broad Line Region in the vicinity of the accreting supermassive black hole. Since GN-z11 is also hosting an AGN, we investigated whether the continuum excess has the same origin as the small blue bump by fitting the continuum excess using a combination of a Balmer continuum and Fe II emission. We summarize our findings in the following.

- A Balmer continuum alone cannot fit the continuum excess due to the significantly blueshifted jump of the continuum excess with respect to the Balmer limit. This indicates that the continuum excess in GN-z11 is not dominated by the Balmer continuum and that the Balmer continuum, if exists, is intrinsically weak.
- The weakness of the Balmer continuum implies part of the Balmer emission should be associated with hot gas at a temperature of $T_e = 2.6^{+0.4}_{-0.6} \times 10^4$ K, which is much higher than the temperature traced by forbidden lines. Hence the Balmer emission likely originates in the dense and hot part of the BLR, while forbidden lines are from the less dense and cool NLR or ISM. We note that, due to the small black hole mass in GN-z11, it is difficult to kinematically distinguish the two components in integrated spectra, as they have similar widths, but they may be separated in spatially resolved spectroscopy.
- While the Fe II emission is typically stronger at $\lambda < 3000$ Å, we explored a series of CLOUDY models and found the Fe II emission at $3000 \text{ \AA} < \lambda < 3550 \text{ \AA}$ can be significantly enhanced under certain conditions. Specifically, our fiducial models that show a prominent Fe II complex within the continuum excess region have $n_H \sim 10^{11} \text{ cm}^{-3}$, $N_H \sim 10^{25} \text{ cm}^{-2}$, $v_{\text{turb}} \sim 600 \text{ km/s}$, $\log(U) \sim -2.5$, and $\log(Z/Z_\odot) \gtrsim -0.5$ or $[\text{Fe}/\text{H}] \gtrsim -0.5$. These Fe II models show a prominent jump around 3500 Å, which can match the observed jump if the Fe II emitting clouds are infalling at a velocity of $\sim 3000 \text{ km/s}$. Still, the Fe II models fail to reproduce the middle part of the jump due to the gaps in the models. Continuum/emission-line fluorescence not taken into account by current models might lead to this mismatch. Future modeling efforts focusing on the comparisons

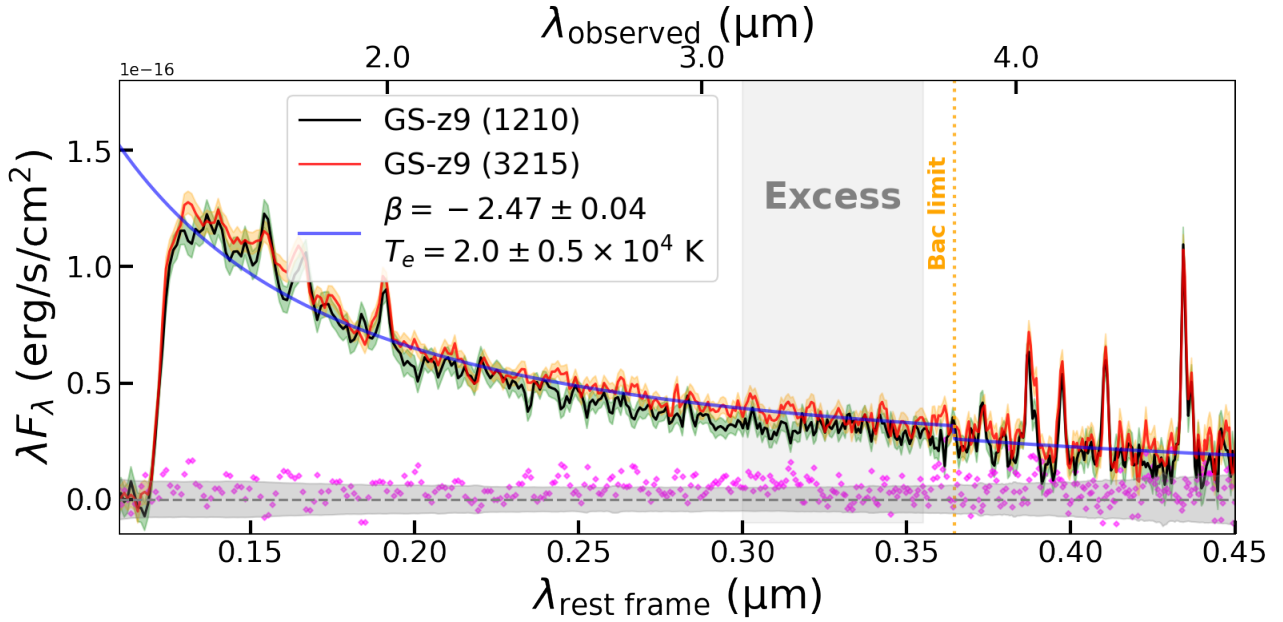


Figure 13. NIRSpec/Prism spectra of JADES-GS-z9-0 from the Cycle 1 Program 1210 and the Cycle 2 Program 3215. The two observations are separated by ~ 1 month in the rest frame of JADES-GS-z9-0. The shaded regions represent 1σ uncertainties of the spectra. The magenta diamonds are the differences between the fluxes the two spectra. The horizontal grey shaded band indicates the 1σ uncertainty of the spectral difference. The blue line is a fit to the continuum of the JADES-GS-z9-0 in 3215 using a power-law function and an optically thin Balmer continuum model. The vertical grey shaded band indicates the continuum excess region in 1210. The orange dotted line indicates the location of the Balmer limit at 3646 \AA .

between models and observations between 3000 \AA and 3550 \AA are needed to fully solve this problem.

- The redshifted Fe II emission was also observed previously in low-redshift quasars, with the highest velocity shift reaching 3000 km/s . A potential explanation is that Fe II emission in BLRs is usually associated with infalling clouds with large column densities viewed from the shielded faces. The minimum column density required to drive the inflow is $\sim 7.5 \times 10^{24} \text{ cm}^{-2}$, consistent with the Fe II model we adopted and the likely Compton-thick nature of the BLR in GN-z11, and as inferred for several other AGN at high- z discovered by JWST (Maiolino et al. 2024a).

- The density of the Fe II models is consistent with the density inferred from high ionization lines, indicating their common origins in the BLR. On the other hand, the seemingly enriched Fe abundance could either be due to the fast enrichment of the overall chemical abundances within the small BLR, or result from a high Fe/O enriched by Type-Ia supernovae or massive HNe/PISNe in the nuclear region.

- Typical ISM surrounding young massive stars can neither produce prominent Fe II emission nor a significantly suppressed Balmer continuum. Thus, the existence of the continuum excess further supports the UV spectrum of GN-z11 is dominated by AGN ionization.

- We found a continuum bump at a similar spectral range in another AGN found in JADES, JADES-GS-z9-0. However, the continuum excess in JADES-GS-z9-0 has a slightly different shape. Interestingly, the UV spectrum of JADES-GS-z9-0 shows variability between observations at two different epochs, with the continuum excess disappear under the rising continuum at the later epoch. We speculate the varying continuum is driven by a changing-look AGN. Whether and how the continuum excess responds to the continuum variability could provide further clues on its origin. It is thus important to have follow-up monitoring of the target to verify the variability as well as characterizing its pattern.

We conclude by emphasizing that the presence of this small blue bump in GN-z11 and its peculiar properties demonstrates the need to reexamine previous theoretical models over a less frequently explored spectral regime, using typically subdominant spectral features in lower redshifts, and in an entirely new parameter space. In the meantime, new observational evidence from higher S/N spectra, especially at high spectral resolution and high spatial resolution with the IFU (e.g., $R \sim 2700$ IFU spectroscopy with NIRSpec), are needed to verify the current interpretations on GN-z11, especially the presence of distinct ionized regions and its exotic chemical abundance pattern in the very early Universe.

ACKNOWLEDGEMENTS

XJ, RM, FDE, JS, and JW acknowledge ERC Advanced Grant 695671 “QUENCH” and support by the Science and Technology Facilities Council (STFC) and by the UKRI Frontier Research grant RISEandFALL. RM acknowledges funding from a research professorship from the Royal Society. JC acknowledges funding from the “FirstGalaxies” Advanced Grant from the European Research Council (ERC) under the European Union’s Horizon 2020 research and innovation programme (Grant agreement No. 789056). ECL acknowledges support of an STFC Webb Fellowship (ST/W001438/1). BER acknowledges support from the NIR-Cam Science Team contract to the University of Arizona, NAS5-02015, and JWST Program 3215. B.R.P. acknowledges support from the research project PID2021-127718NB-I00 of the Spanish Ministry of Science and Innovation/State Agency of Research (MICIN/AEI/10.13039/501100011033). ST acknowledges support by the Royal Society Research Grant G125142. The research of CCW is supported by NOIRLab, which is managed by the Association of

Universities for Research in Astronomy (AURA) under a cooperative agreement with the National Science Foundation.

DATA AVAILABILITY

The JWST/NIRSpec data used in this paper are available through the MAST portal. All analysis results of this paper will be shared on reasonable request to the corresponding author.

REFERENCES

- Abbott D. C., Conti P. S., 1987, *ARA&A*, **25**, 113
- Baldwin J., Ferland G., Korista K., Verner D., 1995, *ApJ*, **455**, L119
- Baldwin J. A., Ferland G. J., Korista K. T., Hamann F., LaCluyz e A., 2004, *ApJ*, **615**, 610
- Berg D. A., Pogge R. W., Skillman E. D., Croxall K. V., Moustakas J., Rogers N. S. J., Sun J., 2020, *ApJ*, **893**, 96
- B oker T., et al., 2023, *PASP*, **135**, 038001
- Bottofff M., Ferland G., Baldwin J., Korista K., 2000, *ApJ*, **542**, 644
- Bottofff M. C., Ferland G. J., Straley J. P., 2006, *PASP*, **118**, 1176
- Bowen I. S., 1934, *PASP*, **46**, 146
- Brightman M., Ueda Y., 2012, *MNRAS*, **423**, 702
- Bunker A. J., et al., 2023a, *arXiv e-prints*, p. [arXiv:2306.02467](https://arxiv.org/abs/2306.02467)
- Bunker A. J., et al., 2023b, *A&A*, **677**, A88
- Byrne C. M., Stanway E. R., Eldridge J. J., McSwiney L., Townsend O. T., 2022, *MNRAS*, **512**, 5329
- Cameron A. J., Katz H., Witten C., Saxena A., Laporte N., Bunker A. J., 2023a, *arXiv e-prints*, p. [arXiv:2311.02051](https://arxiv.org/abs/2311.02051)
- Cameron A. J., Katz H., Rey M. P., Saxena A., 2023b, *MNRAS*, **523**, 3516
- Cameron A. J., et al., 2023c, *A&A*, **677**, A115
- Cappellari M., 2017, *MNRAS*, **466**, 798
- Cappellari M., Emsellem E., 2004, *PASP*, **116**, 138
- Castellano M., et al., 2024, *arXiv e-prints*, p. [arXiv:2403.10238](https://arxiv.org/abs/2403.10238)
- Conti P. S., Massey P., 1989, *ApJ*, **337**, 251
- Curti M., et al., 2023a, *arXiv e-prints*, p. [arXiv:2304.08516](https://arxiv.org/abs/2304.08516)
- Curti M., et al., 2023b, *MNRAS*, **518**, 425
- Dietrich M., Hamann F., Appenzeller I., Vestergaard M., 2003, *ApJ*, **596**, 817
- Dors O. L., Maiolino R., Cardaci M. V., H agele G. F., Krabbe A. C., P erez-Montero E., Armah M., 2020, *MNRAS*, **496**, 3209
- Eisenstein D. J., et al., 2023a, *arXiv e-prints*, p. [arXiv:2306.02465](https://arxiv.org/abs/2306.02465)
- Eisenstein D. J., et al., 2023b, *arXiv e-prints*, p. [arXiv:2310.12340](https://arxiv.org/abs/2310.12340)
- Ferland G. J., Hu C., Wang J.-M., Baldwin J. A., Porter R. L., van Hoof P. A. M., Williams R. J. R., 2009, *ApJ*, **707**, L82
- Ferland G. J., et al., 2017, *Rev. Mex. Astron. Astrofis.*, **53**, 385
- Ferruit P., et al., 2022, *A&A*, **661**, A81
- Foreman-Mackey D., Hogg D. W., Lang D., Goodman J., 2013, *PASP*, **125**, 306
- Furtak L. J., et al., 2023, *arXiv e-prints*, p. [arXiv:2308.05735](https://arxiv.org/abs/2308.05735)
- Gardner J. P., et al., 2023, *PASP*, **135**, 068001
- Garmany C. D., Massey P., Conti P. S., 1984, *ApJ*, **278**, 233
- Gaskell C. M., 1980, *The Observatory*, **100**, 148
- Gaskell M., Thakur N., Tian B., Saravanan A., 2022, *Astronomische Nachrichten*, **343**, e210112
- Gieles M., et al., 2018, *MNRAS*, **478**, 2461
- Goodrich R. W., 1989, *ApJ*, **342**, 224
- Grandi S. A., 1981, *ApJ*, **251**, 451
- Grandi S. A., 1982, *ApJ*, **255**, 25
- Greene J. E., et al., 2023, *arXiv e-prints*, p. [arXiv:2309.05714](https://arxiv.org/abs/2309.05714)
- Grevesse N., Asplund M., Sauval A. J., Scott P., 2010, *Ap&SS*, **328**, 179
- Grogin N. A., et al., 2011, *ApJS*, **197**, 35
- Guo Y., et al., 2020, *ApJ*, **898**, 26
- Hamann F., Ferland G., 1993, *ApJ*, **418**, 11
- Hu C., Wang J.-M., Ho L. C., Chen Y.-M., Bian W.-H., Xue S.-J., 2008a, *ApJ*, **683**, L115
- Hu C., Wang J.-M., Ho L. C., Chen Y.-M., Zhang H.-T., Bian W.-H., Xue S.-J., 2008b, *ApJ*, **687**, 78
- Isobe Y., et al., 2022, *ApJ*, **925**, 111
- Isobe Y., et al., 2023, *ApJ*, **959**, 100
- Jakobsen P., et al., 2022, *A&A*, **661**, A80
- Jenkins E. B., 2009, *ApJ*, **700**, 1299
- Ji X., et al., 2024, *arXiv e-prints*, p. [arXiv:2404.04148](https://arxiv.org/abs/2404.04148)
- Juarez Y., Maiolino R., Mujica R., Pedani M., Marinoni S., Nagao T., Marconi A., Oliva E., 2009, *A&A*, **494**, L25
- Kallman T., McCray R., 1980, *ApJ*, **242**, 615
- Kastner S. O., Bhatia A. K., 1996, *MNRAS*, **279**, 1137
- Kewley L. J., Nicholls D. C., Sutherland R. S., 2019, *ARA&A*, **57**, 511
- Kocevski D. D., et al., 2023, *ApJ*, **954**, L4
- Koekemoer A. M., et al., 2011, *ApJS*, **197**, 36
- Kojima T., et al., 2021, *ApJ*, **913**, 22
- Komossa S., 2008, in *Revista Mexicana de Astronomia y Astrofísica Conference Series*. pp 86–92 ([arXiv:0710.3326](https://arxiv.org/abs/0710.3326)), [doi:10.48550/arXiv.0710.3326](https://doi.org/10.48550/arXiv.0710.3326)
- Kova evi c J., Popovi c L.  ., Kollatschny W., 2014, *Advances in Space Research*, **54**, 1347
- Lai S., Onken C. A., Wolf C., Bian F., Fan X., 2024, *MNRAS*, **527**, 3912
- Lanzuisi G., et al., 2018, *MNRAS*, **480**, 2578
- Laseter I. H., et al., 2023, *arXiv e-prints*, p. [arXiv:2306.03120](https://arxiv.org/abs/2306.03120)
- Leighly K. M., 1999, *ApJS*, **125**, 317
- Luridiana V., Morisset C., Shaw R. A., 2015, *A&A*, **573**, A42
- MacLeod C. L., et al., 2019, *ApJ*, **874**, 8
- Maiolino R., Mannucci F., 2019, *A&ARv*, **27**, 3
- Maiolino R., et al., 2023a, *arXiv e-prints*, p. [arXiv:2306.00953](https://arxiv.org/abs/2306.00953)
- Maiolino R., et al., 2023b, *arXiv e-prints*, p. [arXiv:2308.01230](https://arxiv.org/abs/2308.01230)
- Maiolino R., et al., 2024a, *arXiv e-prints*, p. [arXiv:2405.00504](https://arxiv.org/abs/2405.00504)
- Maiolino R., et al., 2024b, *Nature*, **627**, 59
- Malkan M. A., Sargent W. L. W., 1982, *ApJ*, **254**, 22
- Matsuoka K., Nagao T., Maiolino R., Marconi A., Taniguchi Y., 2009, *A&A*, **503**, 721
- Matsuoka K., Nagao T., Marconi A., Maiolino R., Taniguchi Y., 2011, *A&A*, **527**, A100
- Matsuoka K., Nagao T., Marconi A., Maiolino R., Mannucci F., Cresci G., Terao K., Ikeda H., 2018, *A&A*, **616**, L4
- Matthee J., et al., 2023, *arXiv e-prints*, p. [arXiv:2306.05448](https://arxiv.org/abs/2306.05448)
- Mazzolari G., et al., 2024, *arXiv e-prints*, p. [arXiv:2404.10811](https://arxiv.org/abs/2404.10811)
- Mej a-Restrepo J. E., Trakhtenbrot B., Lira P., Netzer H., Capellupo D. M., 2016, *MNRAS*, **460**, 187
- Nagao T., Marconi A., Maiolino R., 2006a, *A&A*, **447**, 157
- Nagao T., Maiolino R., Marconi A., 2006b, *A&A*, **447**, 863
- Netzer H., Wills B. J., 1983, *ApJ*, **275**, 445
- Netzer H., Elitzur M., Ferland G. J., 1985, *ApJ*, **299**, 752
- Neugebauer G., Oke J. B., Becklin E. E., Matthews K., 1979, *ApJ*, **230**, 79
- Oesch P. A., et al., 2016, *ApJ*, **819**, 129
- Onoue M., et al., 2023, *ApJ*, **942**, L17
- Osterbrock D. E., Pogge R. W., 1985, *ApJ*, **297**, 166
- Peimbert M., 1967, *ApJ*, **150**, 825
- Peimbert M., Peimbert A., Delgado-Inglada G., 2017, *PASP*, **129**, 082001
- Penston M. V., 1987, *MNRAS*, **229**, 1P
- Richstone D. O., Schmidt M., 1980, *ApJ*, **235**, 361
- Rigby J., et al., 2023, *PASP*, **135**, 048001
- Sanders R. L., Shapley A. E., Topping M. W., Reddy N. A., Brammer G. B., 2023a, *arXiv e-prints*, p. [arXiv:2303.08149](https://arxiv.org/abs/2303.08149)
- Sanders R. L., Shapley A. E., Topping M. W., Reddy N. A., Brammer G. B., 2023b, *ApJ*, **955**, 54
- Sarkar A., et al., 2021, *ApJ*, **907**, 12
- Schmidt G. D., Miller J. S., 1980, *ApJ*, **240**, 759
- Scholtz J., et al., 2023a, *arXiv e-prints*, p. [arXiv:2306.09142](https://arxiv.org/abs/2306.09142)
- Scholtz J., et al., 2023b, *arXiv e-prints*, p. [arXiv:2311.18731](https://arxiv.org/abs/2311.18731)
- Senchyna P., Plat A., Stark D. P., Rudie G. C., 2023, *arXiv e-prints*, p. [arXiv:2303.04179](https://arxiv.org/abs/2303.04179)
- Shields G. A., Ludwig R. R., Salviander S., 2010, *ApJ*, **721**, 1835
- Stanway E. R., Eldridge J. J., 2018, *MNRAS*, **479**, 75
- Tacchella S., et al., 2023a, *MNRAS*, **522**, 6236

- Tacchella S., et al., 2023b, *ApJ*, **952**, 74
 Tacchella S., et al., 2024, *arXiv e-prints*, p. [arXiv:2404.02194](https://arxiv.org/abs/2404.02194)
 Temple M. J., Ferland G. J., Rankine A. L., Chatzikos M., Hewett P. C., 2021, *MNRAS*, **505**, 3247
 Topping M. W., et al., 2024, *MNRAS*, **529**, 3301
 Tszuki Y., Kawara K., Yoshii Y., Oyabu S., Tanabé T., Matsuoka Y., 2006, *ApJ*, **650**, 57
 Übler H., et al., 2023a, *arXiv e-prints*, p. [arXiv:2312.03589](https://arxiv.org/abs/2312.03589)
 Übler H., et al., 2023b, *A&A*, **677**, A145
 Ulrich M. H., et al., 1980, *MNRAS*, **192**, 561
 Ulrich M.-H., Maraschi L., Urry C. M., 1997, *ARA&A*, **35**, 445
 Vanden Berk D. E., et al., 2001, *AJ*, **122**, 549
 Vanni I., Salvadori S., Skúladóttir Á., Rossi M., Koutsouridou I., 2023, *MNRAS*, **526**, 2620
 Verner E. M., Verner D. A., Korista K. T., Ferguson J. W., Hamann F., Ferland G. J., 1999, *ApJS*, **120**, 101
 Vernet J., et al., 2011, *A&A*, **536**, A105
 Véron-Cetty M. P., Véron P., Gonçalves A. C., 2001, *A&A*, **372**, 730
 Vestergaard M., Wilkes B. J., 2001, *ApJS*, **134**, 1
 Watanabe K., et al., 2024, *ApJ*, **962**, 50
 Wills B. J., Netzer H., Wills D., 1985, *ApJ*, **288**, 94
 Witstok J., Smit R., Maiolino R., Curti M., Laporte N., Massey R., Richard J., Swinbank M., 2021, *MNRAS*, **508**, 1686
 Wu Q., Shen Y., 2022, *ApJS*, **263**, 42
 York D. G., et al., 2000, *AJ*, **120**, 1579
 de Graaff A., et al., 2023, *arXiv e-prints*, p. [arXiv:2308.09742](https://arxiv.org/abs/2308.09742)

APPENDIX A: DETECTION OF THE SMALL BLUE BUMP IN JACKKNIFED PRISM SPECTRA

To check whether the small blue bump in the Prism spectrum of GN-z11 is caused by any detector artefact during observations, we Jackknifed the Prism spectra from independent measurements.

The May observation of GN-z11 has 7 unique MSA positions and a total of 9 exposures. We considered exposures with the same shutter position as an independent trial, which results in 7 trials for the May observation. Similarly, we identified 12 trials from a total of 24 exposures in February. In total, we have 19 measurements for Jackknifing.

Figures A1 and A2 show the 19 Jackknifed spectra from the measurements. Each spectrum was obtained by excluding one measurement and combining the rest of the measurements through inverse-variance weighting and $3\text{-}\sigma$ clipping. It is clear that the continuum excess in the near-UV as well as the jump near 3550 \AA persists in all Jackknifed spectra, confirming it is not an artefact driven by a single measurement. Meanwhile, the emission at 3133 \AA is also visible in all the spectra. In contrast, a potential emission line at $\sim 3300 \text{ \AA}$ seemed disappeared when measurement 16 was excluded, meaning it is mainly from this measurement.

APPENDIX B: OPTICALLY THICK BALMER JUMP CASE

In this Appendix we describe an attempt to fit the small blue bump by assuming a partially optically thick Balmer continuum, which includes an additional free parameter, the optical depth at the Balmer edge, τ_{BC} . This model was initially proposed by Grandi (1982) to describe line-emitting clouds that are heated towards large optical depths in quasars.

A partially optically thick Balmer continuum is increasingly suppressed at longer wavelengths due to the cubic dependence of the absorption cross section on the wavelength. Figure B1 shows the best-fit model with $T_e = 5.2^{+1.3}_{-1.0} \times 10^3 \text{ K}$ and $\tau_{\text{BE}} = 4.4^{+3.7}_{-2.7}$. While

the model has a similar shape to that of the model in the optically thin limit, the best-fit temperature is significantly lower and it is atypical for photoionized gas. This is due the normalization of the Balmer edge is set as a free parameter. There exists a degeneracy between the normalization of the Balmer edge and the optical depth. In practice, the temperature is usually fixed to a typical value when adopting this flexible model (Grandi 1982). It is clear that even with a partially black-body component and (possibly unphysical) freedom to vary the normalization of the Balmer continuum, the Balmer continuum cannot fully recover the shape of the small blue bump.

APPENDIX C: Fe II JUMP IN QUASAR SPECTRA

In this Appendix we show a few more examples of quasar spectra that exhibit UV jumps bluewards of the Balmer limit caused by Fe II emission. These quasars were selected from a sample of luminous quasars at $4.5 < z < 5.3$ in the XQz5 catalog compiled by Lai et al. (2024). The spectra were obtained with X-shooter (Vernet et al. 2011) at the Very Large Telescope (VLT). These quasars have prominent UV continuum emission and their Eddington ratios are on average 0.3 dex higher than the lower-redshift quasars in SDSS with similar black hole masses (Wu & Shen 2022; Lai et al. 2024).

APPENDIX D: VOLUME-AVERAGE ELECTRON TEMPERATURES IN DIFFERENT IONIZED CLOUDS

Figure D1 shows the CLOUDY predictions on the volume-average $T_e(\text{H}^+)$ for clouds ionized by young stars and AGNs, respectively. For SF clouds, we adopted a fiducial model which uses the Binary Population and Spectral Synthesis models (BPASS; Stanway & Eldridge 2018; Byrne et al. 2022) assuming 1 Myr after a burst of star formation. Even with $\log(U) = -1$ and $\log(Z/Z_\odot) = -3$, the volume-average $T_e(\text{H}^+)$ is still lower than $3 \times 10^4 \text{ K}$. In comparison, a low-density NLR can reach $T_e(\text{H}^+) \sim 3 \times 10^4 \text{ K}$ at a fiducial metallicity of $\log(Z/Z_\odot) = -0.84$ inferred for GN-z11 (Cameron et al. 2023b) and a $\log(U)$ between -1.5 and -1 . At such a high temperature, however, the electron temperature traced by $[\text{O III}]\lambda 4363$ in the NLR would be comparably high, which is inconsistent with what we observed in GN-z11.

Finally, for high-density BLR models, we calculate the volume-average temperature, $T_e(\text{H}^+)$, within a column density of $N_{\text{H}} = 10^{22} \text{ cm}^{-2}$ at a fiducial density of $n_{\text{H}} = 10^{11} \text{ cm}^{-3}$, which roughly encloses the H^+ zone for the range of ionization parameters we considered (Ferland et al. 2009). While the above parameters can produce $T_e(\text{H}^+) \sim 3 \times 10^4 \text{ K}$ at $\log(Z/Z_\odot) \sim -1$ and $\log(U) \sim -1$, it is possible for other combinations of n_{H} and N_{H} to achieve high temperatures.

This paper has been typeset from a $\text{\TeX}/\text{\LaTeX}$ file prepared by the author.

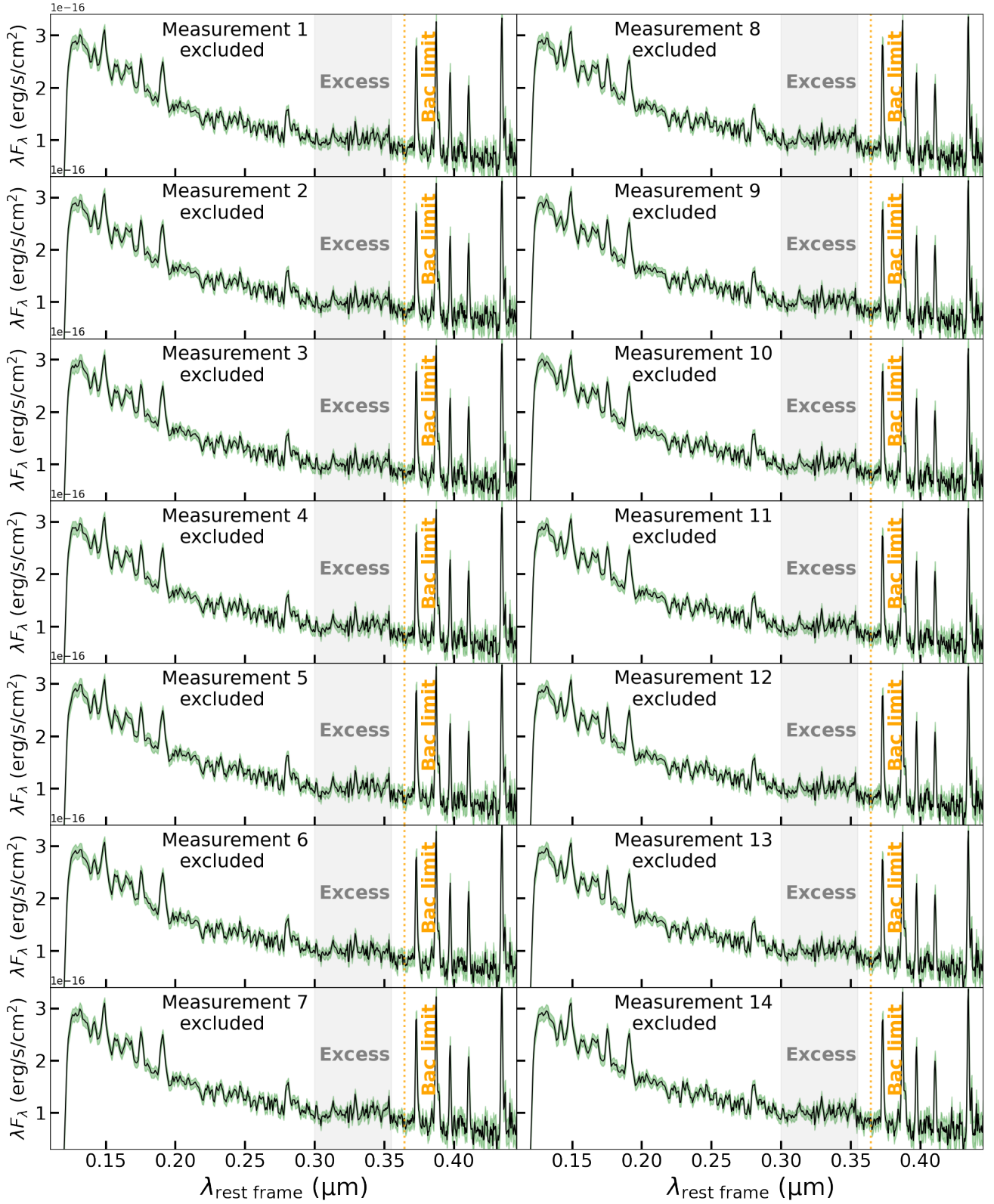


Figure A1. Jackknifed Prism spectra of GN-z11 generated from a total of 19 measurements. For each panel, one of the measurements is excluded and the rest of the measurements is combined via an inverse-variance weighted method with $3\text{-}\sigma$ clipping. The green shaded regions indicate the combined 1σ uncertainties. The grey shaded region marks the continuum excess region identified in the final spectrum combining all measurements. The orange dotted line marks the location of the Balmer continuum limit. The first 14 Jackknifed spectra are shown.

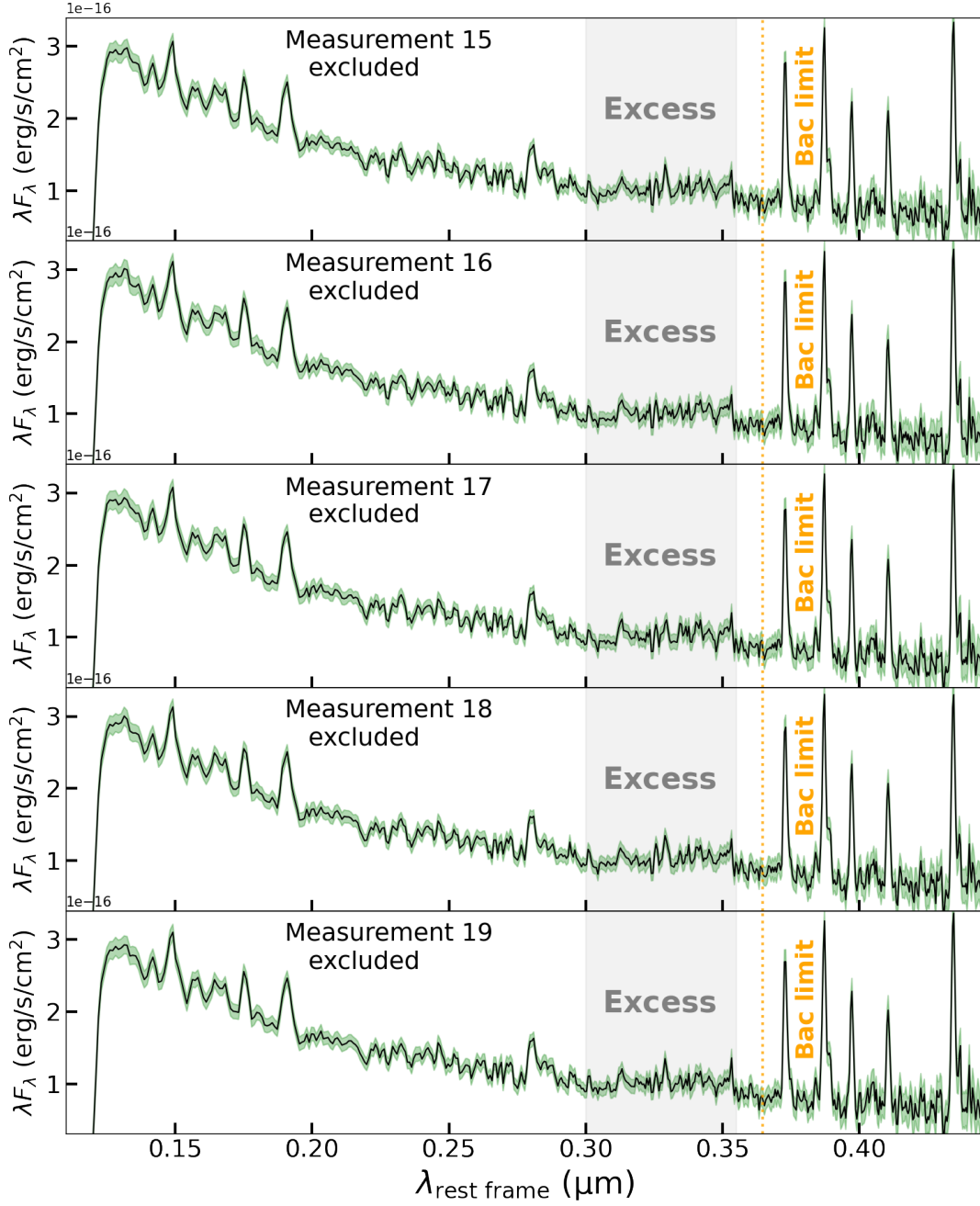


Figure A2. Jackknifed Prism spectra of GN-z11 generated from a total of 19 measurements. The remaining 5 Jackknifed spectra are shown.

Table B1. Best-fit model parameters for the GN-z11 continuum

Assumption	Power law (PL)	Balmer continuum (BC)	Fe II emission (FeII)
PL + BC (optically thin)	$\beta = -2.37 \pm 0.02$	$T_e = 1.69^{+2.9}_{-2.3} \times 10^4$ K	N/A
PL + BC (partially optically thick)	$\beta = -2.27 \pm 0.02$	$T_e = 5.2^{+1.3}_{-1.0} \times 10^3$ K $\tau_{BE} = 4.4^{+3.7}_{-2.7}$	N/A
PL + BC (suppressed) + FeII	$\beta = -2.27 \pm 0.02$	$T_e = 2.6^{+0.4}_{-0.6} \times 10^4$ K	$\log(Z/Z_\odot) \gtrsim -0.5$ $v_{Fe^+} = 3 \times 10^3$ km/s

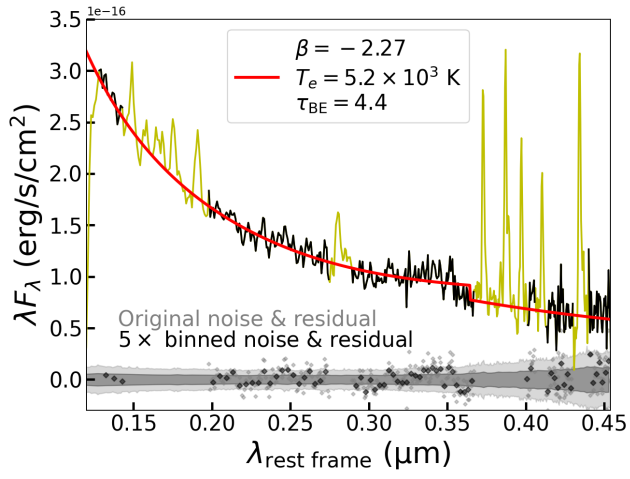


Figure B1. As Fig.2 but where the Balmer continuum has been replaced by the partially optically thick case. In this case the optical depth and the normalization of the Balmer edge were jointly fitted.

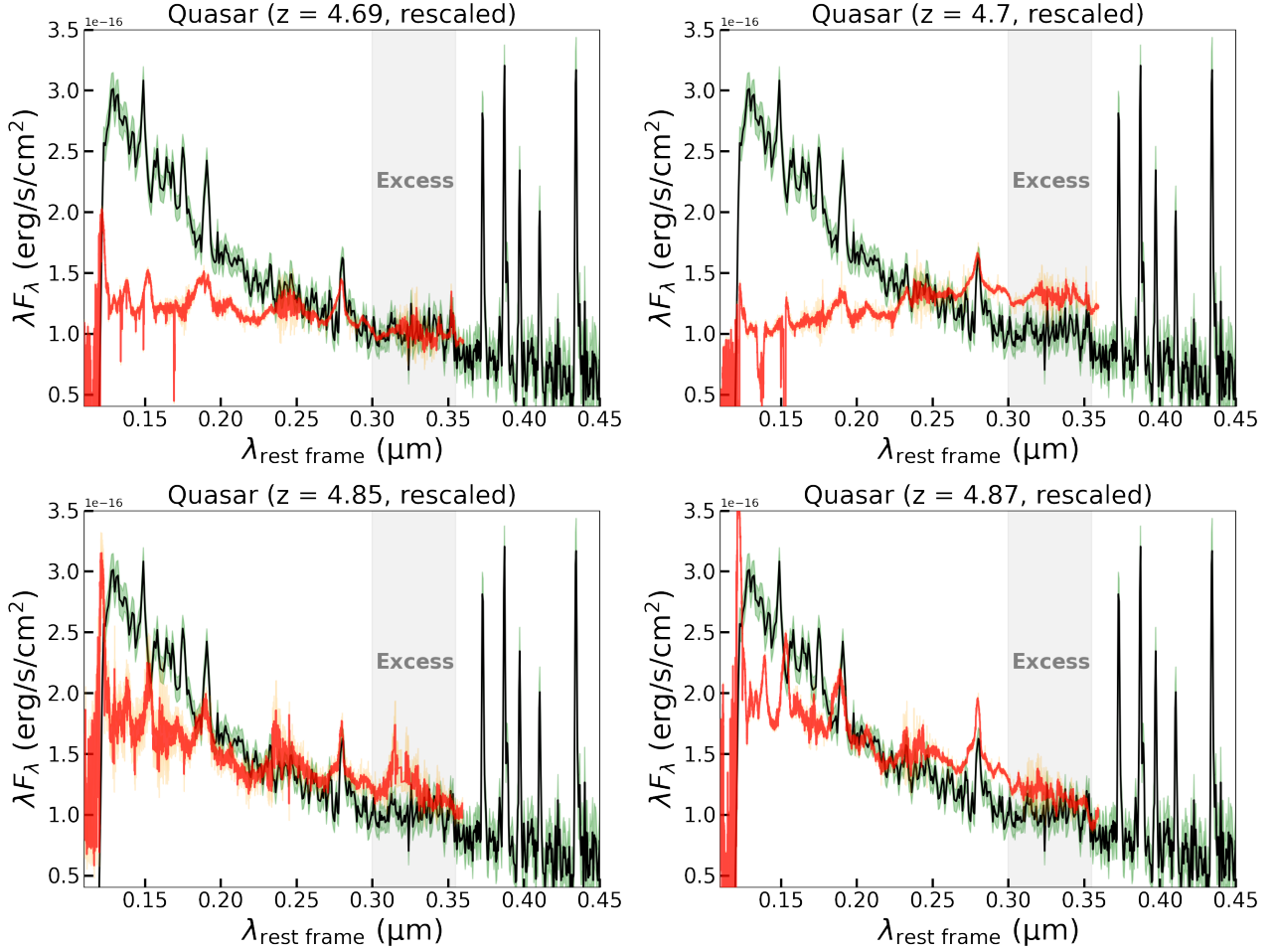


Figure C1. Comparison between the rest-frame UV spectra of quasars from [Lai et al. \(2024\)](#) and that of GN-z11. The quasar spectra are plotted in red with their 1σ uncertainties indicated by the orange shaded region. The fluxes of the quasars are rescaled. The spectrum of GN-z11 is shown in black with the 1σ uncertainty indicated by the green shaded region. The continuum excess region we identified in GN-z11 is highlighted with the grey shaded band.

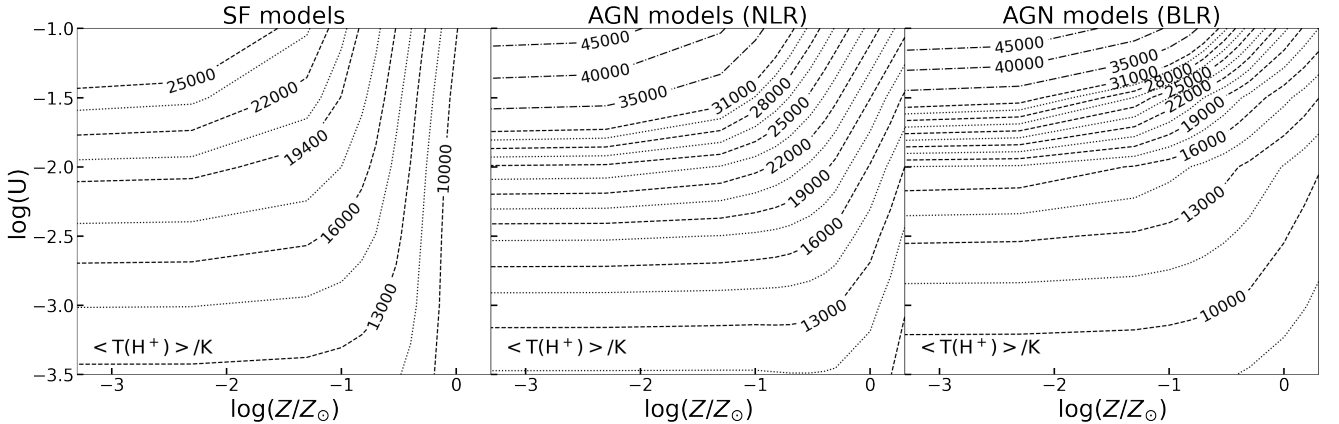


Figure D1. Predictions on hydrogen Balmer temperatures for clouds ionized by different sources as functions of the metallicity and ionization parameter. *Left:* contours of electron temperatures of SF models ionized by a simple stellar population (SSP) from a 1 Myr-old starburst generated by BPASS assuming the default initial mass function (IMF) with an upper mass limit of $300 M_{\odot}$ described in [Stanway & Eldridge \(2018\)](#). Both the dashed lines and dotted lines are plotted with steps of 3000 K. Adjacent dashed lines and dotted lines are separated by 1500 K. *Middle:* contours of electron temperatures of NLR models ionized by an AGN SED the same as the one in Table 1. The hydrogen density of the models is set to 10^3 cm^{-3} . *Right:* contours of electron temperatures of BLR models ionized by an AGN SED the same as the one in Table 1. The hydrogen density of the models is set to 10^{11} cm^{-3} and the hydrogen column density is set to 10^{22} cm^{-2} as appropriate for the H^+ region within the BLR. While the SF models and NLR models include dust depletion, the BLR models do not.